Study of ^{34m}Cl beam production at the National Superconducting Cyclotron Laboratory.

By

Olalekan Abdulqudus Shehu

Approved by:

Benjamin Crider (Major Professor)
Jeff Allen Winger
Dipangkar Dutta
Henk F. Arnoldus (Graduate Coordinator)
Rick Travis (Dean, College of Arts & Sciences)

A Thesis
Submitted to the Faculty of
Mississippi State University
in Partial Fulfillment of the Requirements
for the Degree of Master of Science
in Nuclear Physics
in the Department of Physics and Astronomy

Mississippi State, Mississippi

August 2020

Name: Olalekan Abdulqudus Shehu

Date of Degree: August 7, 2020

Institution: Mississippi State University

Major Field: Nuclear Physics

Major Professor: Benjamin Crider

Title of Study: Study of ^{34m}Cl beam production at the National Superconducting Cyclotron Laboratory.

Pages of Study: 82

Candidate for Degree of Master of Science

The success of many experiments at rare-isotope facilities, such as the National Superconducting Cyclotron Laboratory (NSCL), depends on achieving a level of statistics that is partly driven by the overall number of nuclei produced in the beam. One such future study at the NSCL requires maximizing the beam content of ^{34m}Cl. To prepare for this ^{34m}Cl study, an initial measurement to determine the ^{34m}Cl yields and overall beam purity was performed at the NSCL by utilizing a β-decay experimental station. Isotopes delivered to the experimental station were identified using standard time of flight and energy loss techniques. To explore ways of maximizing ^{34m}Cl production, 6 different beam energy settings that selected different rigidities for isotopic selection and altered its entrance angles before the beam went into the fragment separator, were utilized. The absolute intensity of the peak energies associated with the decay of ^{34m}Cl (1177, 2127, and 3304 keV) were determined, as well as the overall number of ^{34}Cl atoms delivered, thereby enabling ^{34m}Cl yield and beam purity determinations for each beam setting.

Key words: β decay, isomeric state, γ rays

DEDICATION

This thesis is dedicated to my parents Mr. Usman Shehu and Mrs. Nimot Shehu.

ACKNOWLEDGEMENTS

First, I would like to thank my advisor, Dr. Benjamin Crider, for his guidance and support over the past two years and for facilitating my participation in many experiments, particularly this project. His mentorship throughout my graduate studies at the Mississippi State University has helped me position myself in line with what I hope to accomplish in the long run, including the next chapter of my career. His approachability and availability, despite numerous commitments made it easy for me to focus and work efficiently while balancing my coursework and research. It has been an absolute joy working with you. Thank you.

I would also like to acknowledge my guidance thesis committee, Dr. Jeff Allen Winger and Dr. Dipangkar Dutta for their advice, input and availability.

I wish to express my gratitude to Calem Hoffman and Tom Ginter at the National Superconducting Cyclotron Laboratory (NSCL) for providing essential information and direction pertaining to my analysis as well as giving inputs to my thesis.

I also want to thank the National Science Foundation (NSF) for providing the financial support to carryout this work. This work was supported by the National Science Foundation under Grant No. PHY 1848177 (CAREER).

I would like to give a special thanks to Timilehin Ogunbeku for being a friend and an available member of my research group despite his relocation to Michigan. His courteous and friendly nature made my settling down in the Mississippi State University environment an easy one. I

appreciate your reassuring words when I was discouraged and your assistance in obtaining some of the results presented in this thesis. I also wish to thank Yongchi Xiao for his tremendous help in the completion of my analysis. This thesis would be incomplete without both their contributions.

I would be remiss to not acknowledge my fellow graduate students, Daniel Solomon Araya, Sapan Luitel, Udeshika Perera and Nuwan Chaminda. I really did enjoy our hangouts and long talks and I am grateful for the camaraderie among us. I truly value our friendship and it has been a pleasure meeting you all. I wish to thank Daniel Solomon Araya in particular, for a friendship that has helped me through all my exams and for being the best office mate. He provided me with sage advice and direction. Thank you.

Finally, my heartfelt thanks to my parents and siblings, for their incessant love, encouraging words and prayers.

TABLE OF CONTENTS

LIST OF TABLES

LIST OF FIGURES

LIST OF SYMBOLS, ABBREVIATIONS, AND NOMENCLATURE

SeGA Segmented Germanium Array

$CeBr_3$ Cerium Bromide

NSCL National Superconducting Cyclotron Laboratory

PAC Program Advisory Committee

log ft Comparative half life

MeV Mega-electron volt

Z Atomic number

DC Direct current

RF Radiofrequency

CCF Coupled Cyclotron Facility

enA Electrical nano amperes

PPS Particles Per Second

PIN p-n type semiconductor

ToF Time of flight

TKE Total kinetic energy

TAC Time-to-Amplitude-Converter

PID Particle identification

PSPMT Position Sensitive Photo-Multiplier Tube

MCA Multi-channel analyzer

keV Kilo-electron volt

NIST National Institute of Standard and Technology

SRM Standard Reference Material

GEANT4 Toolkit for the simulation of the passage of particles through matter

ISOL Isotope Separation On Line

CHAPTER I

INTRODUCTION

1.1 The atomic nucleus

The atomic nucleus is the dense center of an atom consisting of protons and neutrons, which make up the class of particles known as nucleons. Given that protons are positively charged, it would seem impossible to confine any number of protons within a small volume. The electromagnetic interaction between these positively charged particles should cause them to repel. However, there is force that counteracts the repulsive electromagnetic interaction, thereby enabling a bound system of nucleons to survive. This force is called the strong force [1].

The atomic nucleus was discovered in 1911 by Ernest Rutherford [2], based on Geiger-Marsden gold foil experiment [3]. While there are nearly 300 stable nuclei, there are certain numbers of protons and neutrons, called “magic" numbers (see Sec. 1.3), which have enhanced stability when compared to other nearby nuclei. For a nucleus with too many neutrons or protons, excess energy in the core of the atom gets out of balance. Atoms with such excess energy are called radionuclides which follow some process of radioactive decay to become more stable. Radioactive decay also know as radioactivity is the characteristic behavior of unstable nuclei spontaneously decaying to different nuclei and emitting radiation in the form of particles or high energy photons.

The discovery of radioactivity took place over several years beginning with the detection of X-rays by Wilhelm Conrad Röentgen while conducting experiments on the effect of cathode rays.

He placed an experimental electric tube upon a book beneath which was a photographic plate. Later, he used the plate in his camera and was puzzled upon developing it, to find the outline of a key on the plate. He searched through the same book and discovered a key between the pages. The "strange" light from the glass tube had penetrated the pages of the book; thus, X-rays were discovered [4]. Following the discovery of X-rays, Henri Becquerel in 1896 used natural fluorescent minerals to study the properties of X-rays. This process involved exposing potassium uranyl sulfate to sunlight and then placing it on a photographic plate wrapped in black paper. In this hypothesis, he believed that the uranium will absorb the sun's energy and then emit X-rays, but his experiment failed due to an overcast sky in Paris. For some reason, Becquerel decided to develop his photographic plate anyway by placing it in a dark drawer. Surprisingly, the images were strong and clear proving that radiation was emitted from the uranium without an external source of energy such as the sun. Becquerel had discovered radioactivity [5]. Not long after, French physicists Pierre and Marie Curie extracted uranium from uranium ores and found the leftovers still showed radioactivity. This led to the discovery of polonium and radium. Marie Curie coined the term radioactivity for the spontaneous emission of ionizing rays by certain atoms. Marie and Pierre Curie were awarded half the Nobel Prize in recognition for the joint research on radiation. The other half was awarded to Henri Becquerel for his spontaneous radioactive discovery [6].

1.2 Binding energy

In order to quantify which nuclei decay and why, one property that can be utilized is the so-called "binding energy" of the nucleus. Binding energy (BE) of a nucleus is the energy required to

separate the nucleus of an atom into protons and neutrons. The general expression for the binding energy requires Einstein's famous relationship equating rest mass to energy given by

$$E = mc^2 \tag{1.1}$$

where m is the rest mass and c is the speed of light. The rest mass is used to determine the binding energy of a nucleus [7]. Another important quantity is the average energy used to remove a single nucleon from a nucleus. This quantity is called the binding energy per nucleon, and is represented by

$$BE = \frac{E_\mathrm{b}}{A} \tag{1.2}$$

where E_b is the binding energy and A is the number of nucleons [7].

At the nuclear level, the nuclear binding energy is the energy required to separate the components of the nucleus by overcoming the strong nuclear force. The nuclear binding energy is given by

$$E_\mathrm{b}({}^{A}_{Z}X_\mathrm{N}) = [ZM_\mathrm{H} + NM_\mathrm{n} - M({}^{A}_{Z}X_\mathrm{N})]c^2 \tag{1.3}$$

where Z is the atomic number, M_H is the mass of the hydrogen nucleus (proton), N is the neutron number, M_n is the neutron mass, $M({}^{A}_{Z}X_\mathrm{N})$ is the atomic mass of the given nucleus [8].

In general, for a nucleus to be bound, the binding energy needs to be positive according to Eq. 1.3. The more stable a nucleus, the higher the binding energy. Radioactivity decay therefore occurs when a more tightly bound nucleus can be obtained.

1.3 The nuclear shell model

In the course of the study of atomic nuclei, the idea of a shell structure began to emerge. This shell structure is analogous to the shell structure of an electrons orbital in an atom, but also

has several differences. One way to illustrate the shell structure phenomenon in atoms is with ionization energy, which is the energy required to remove the most loosely bound electron. The ionization energy as a function of atomic number, Z, exhibited discontinuities as shown in Fig. 1.1 (left). The discovery of these discontinuities proved that the atom existed in electronic shells [1]. The discontinuities emerged from the underlying shell structure. In the process of filling electrons in orbital shells, the energy is reduced considerably when the next electron is placed in a higher energy orbital.

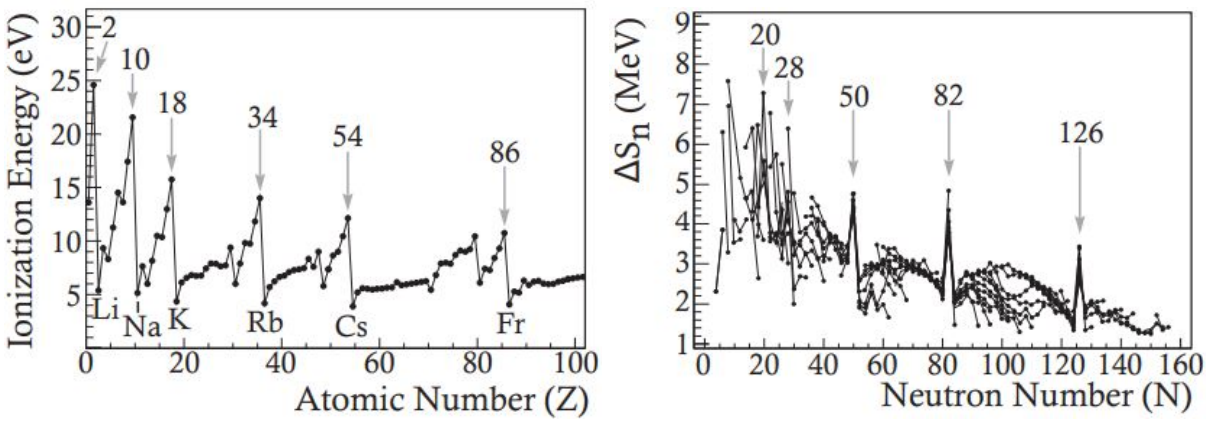

Figure 1.1: (Left) First ionization energies of the atomic elements from hydrogen (Z=1) to nobelium (Z=102). (Right) Differences in neutron separation energy for even-even nuclei and their even-odd neighbors. Figure from Ref. [8].

In the nuclear system, trends in the nuclear mass and binding energy have proved increased stability for nuclei associated with "magic" numbers corresponding to when the proton or neutron number equals 2, 8, 20, 28, 50, 82 and 126. Therefore, making the nuclear shell model analogous to the atomic shell model. These numbers led to the development of the shell model, where the

magic numbers corresponds to the filling of major nuclear shells [1]. To compare to the ionization energy in atoms, we can utilize the neutron separation energy (S_{n}), which is the energy required to remove a single neutron from the nucleus. The neutron separation energy is defined as

$$S_{\mathrm{n}}(N) = E_{\mathrm{b}}({}^{A}_{Z}X_{\mathrm{N}}) - B({}^{A-1}_{Z}X_{\mathrm{N\text{-}1}}) = [M({}^{A-1}_{Z}X_{\mathrm{N\text{-}1}}) - M({}^{A}_{Z}X_{\mathrm{N}}) + M_{\mathrm{n}}]c^2 \tag{1.4}$$

Here $E_{\mathrm{b}}({}^{A}_{Z}X_{\mathrm{N}})$ is represented by Eq. 1.3. Similarities between the neutron separation energy and the atomic ionization energy are apparent due to the neutron separation energy showing periodicity, suggesting a nuclear shell structure.

The nuclear shell structure can be corroborated by describing the even N nuclei and their $N+1$ neighbors in terms of the change in S_{n}:

$$\triangle S_{\mathrm{n}} = S_{\mathrm{n}}(N) - S_{\mathrm{n}}(N+1) = [M({}^{A-1}_{Z}X_{\mathrm{N\text{-}1}} + M({}^{A-1}_{Z}X_{\mathrm{N+1}}) - 2M({}^{A}_{Z}X_{\mathrm{N}}))]c^2 \tag{1.5}$$

Fig. 1.1 (Right) shows the differences in neutron separation energy for even-even nuclei and their even-odd neighbors up to fermium (Z=100). Similar to the electron ionization energy, the observed discontinuities underscores the neutron magic numbers [8].

The ability of the nuclear shell model to describe the observed behavior depends on the choice of the potential which confines the protons and neutrons within the nucleus. Historically, theorists tried to reproduce the magic numbers by utilizing several mathematical formalisms [1, 8]. A harmonic oscillator potential was first considered. Solving the Schrödinger equation describes the energy levels of a harmonic oscillator potential as shown in Fig. 1.2 (Right). The lowest shell closures at 2, 8, and 20 were reproduced correctly by the harmonic oscillator potential but the higher level shell closures were in disagreement. This is because it had an unrealistic potential (V

$\rightarrow \infty$) at the boundary of the nucleus [1]. Similar issues come up when considering the infinite well potential (see Fig. 1.2) (Left).

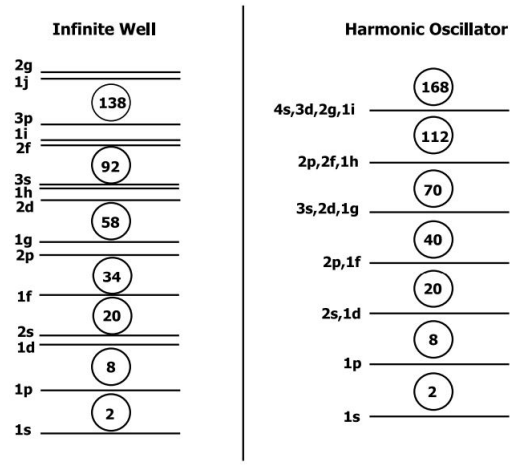

Figure 1.2: Nuclear shell structure considering the infinite well potential (Left) and harmonic oscillator potential (Right). Figure from Ref. [1].

The Woods-Saxon potential was considered next because it provides a much better approximation at $r = R$ (nucleons near the surface of a nucleus). It takes the form

$$V(r) = \frac{-V_0}{1 + \exp[\frac{(r-R)}{a}]} \tag{1.6}$$

where r is the distance from the center of the nucleus, R is the mean nuclear radius (1.25 fm $A^{1/3}$), a is the surface thickness of the nucleus and V_0 is the depth of the potential. Typical values for the Wood Saxon potential depth are $V_o \sim 50$ MeV. As shown in Fig. 1.3 (Left), this potential reproduces the magic numbers 2, 8 and 20, but fails for numbers beyond.

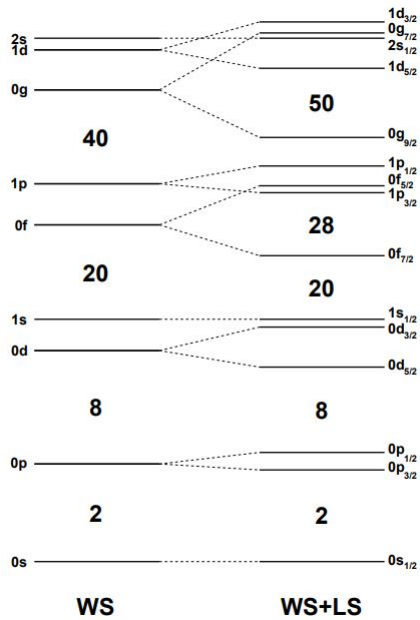

Figure 1.3: Wood-Saxon potential is the spectrum labeled WS. The spectrum labeled WS+LS includes the spin-orbit term. Figure from Ref. [9].

In the 1940's, it was discovered that adding a spin-orbit potential to the Wood-Saxon potential allowed the theory to reproduce all of the observed magic numbers [10, 11]. The spin-orbit potential is represented by

$$V_{\mathrm{so}} = V_{\mathrm{so}}(r)\vec{l}\cdot\vec{s} \tag{1.7}$$

where $V_{\mathrm{so}}(r)$ is a radially dependent strength constant, $\vec{l}$ is the orbital angular momentum and $\vec{s}$ is the intrinsic nucleon spin. The term $\vec{l}\cdot\vec{s}$ describes the orbital motion and nuclear spin interactions, and leads to a removal of the l-degeneracy states, or a splitting of states with l>0. This results is shown in Fig. 1.3 (right) [1, 8]. Additionally, the spin-orbit splitting increases with angular momentum causing the higher-j state to be pushed into a group of states from a lower shell. This is how the higher magic numbers are obtained.

From Fig. 1.3, the $^{2S+1}L_j$ spectroscopic notation is used to describe the energy levels where S is the spin, L is the orbital angular momentum and j is the total angular momentum. The number of nucleons a shell can hold is 2j+1. For example, $^0P_{3/2}$ has a spin of -1/2, has a L=1, and a total of 4 nucleons. The sd region adds 6, 4, 2 number of nucleons respectively to the existing magic number of 8. Following this filling, there is a shell gap before moving into the fp region. The fp region begins its filling with 8 nucleons, therefore leaving a shell gap. Finally the fp shell fills up with a 4, 6, 2 nucleon numbers corresponding to $^1P_{3/2}$, $^0f_{5/2}$, and $^1P_{1/2}$. The isotope of interest ^{34}Cl, which has 17 protons and 17 neutrons, would have its ground state in the fp region.

1.4 Nuclear deformation

Nuclear deformation is a central concept to understanding nuclear structure [12]. Since an understanding about the forces that shape the nucleus is incomplete, no theory has succeeded to explain the properties of the nuclear structure wholly. Nuclear deformation depends on the Coulomb force, the nuclear force and the shell effects. The atomic nucleus exhibits spherical, quadrupole and higher-order multipole deformations [13].

Nuclei having deformation generally are classified into prolate, oblate, and triaxial. Prolate and oblate nuclei are axially symmetric. This means the appearance is unchanged if rotated around an axis. If the third axis of the nucleus is longer than the others, the nucleus is prolate and if it is shorter, the nucleus is oblate. All three axes are different for triaxial nuclei [13].

The deformation of a nucleus impacts many observables. Beyond direct effects of impacting level energies and transition strengths within excited states of a nucleus, deformation can also impact cross-sections relevant to astrophysical processes such as the rapid proton capture nucleosynthesis

process which will be defined later in Sec. 1.5. One example is the enhancement of (n, γ) cross sections for many nuclei on the s-process and r-process path due to dipole deformation that can affect the overall trajectory of these processes [14].

1.5 Goals of the experiment

The physics motivation of the experiment 16032A is to study the ^{34m}Cl yields and overall beam purity at the NSCL. The application of this knowledge will be used for an experiment in studying the single-neutron occupancies of the excitation energies between analog states of mirror nuclei (atomic nuclei that contains a number of protons and a number of neutron that are interchanged) which is called the Mirror Energy Difference (MED). MED's probe the charge independence and symmetry of nuclear strong force. This measurement will be focused on the high MEDs states of ^{35}Cl and ^{35}Ar. The states of interest can be populated with an high probability by adding a neutron into the isomeric state of ^{34}Cl. ^{34g,m}Cl (d,$p\gamma$) reaction is further required to populate the states of interest. The ^{34g,m}Cl (d,$p\gamma$) reaction begins with a ^{34}Cl beam hitting a deuterium (Proton + neutron) target. This results in a ^{36}Ar compound nucleus for a very brief amount of time($\sim 10^{-22}$ s). Then the ^{36}Ar emits a proton and γ-ray energies and the final reaction is left with the ^{35}Cl isotope. The isomeric state of ^{34}Cl, which has $J^{\pi} = 3^{+}$, is required to enhance the probability for the population of the higher spin ^{35}Cl excited states of interest and this thesis aims to measure the isomeric state yield in a beam of ^{34}Cl produced at the NSCL.

The study of ^{34}Cl also plays an important role in the rp-process (rapid-proton capture) nucleosynthesis. The rp-process nucleosynthesis is the process responsible for the generation of many heavy elements present in the universe. The rp-process consists of consecutive proton capture

onto seed nuclei to produce heavier elements [15]. Uncertainties in the rates for both the ground and isomeric state of ^{34}Cl, translate into uncertainties in ^{34}S production which is an important observable in preosolar grains. Presolar grains are solid grains that started at a time before the sun was formed. The majority of these grains are condensed in the outflow of asymptotic giant branch stars and supernovae [16].

An interesting feature of ^{34}Cl is that it has a low-lying, long-lived isomer, which can complicate its interpreted impact in the aforementioned applications. This isomer, typically labeled as ^{34m}Cl (denoting its characterization as a "meta-stable" state) behaves differently from other isotopes in astrophysical environments. Specifically, the assumption of thermal equilibrium in computing the temperature-dependent β-decay rates can fail below certain temperatures [17]. Therefore, the study of the nuclear structure of ^{34}Cl is crucial in understanding the nuclear reaction codes to calculate the nucleosynthesis that occurs in hot stellar environments.

CHAPTER II

RADIOACTIVE DECAY

There are different forms by which nuclei emit radiation to remove excess energy. The types that are primarily relevant to the nuclei of interest in this work will be discussed here: β decay and γ decay. This chapter also goes into details about the physics governing the decay law, selection rules and the Bateman equation.

2.1 Radioactive decay law

A universal law that describes the statistical behavior of a large number of unstable nuclei is called the radioactive decay law. For an unstable nucleus to release particles, they must overcome the strong nuclear force holding the nucleons together. This implies that the rate of decay varies for different nuclei, which depends on the properties of these individual nuclei such as the number of nucleons, the filling of shells and subshells, and the energy difference between the initial and final states, to name a few.

The radioactive decay law states that the probability per unit time that a decay occurs in the nucleus is a constant denoted by λ, and it is independent of time. Considering N to be the total number of nuclei in a sample and dN to be the change in number of nuclei in the sample in a time dt. The rate at which radioactive nuclei decay is proportional to the decay constant and can be written as

$$\frac{dN}{dt} = -\lambda N \tag{2.1}$$

The constant λ varies amongst different nuclei thereby causing different observed decay rates. Solving this first-order differential equation yields the number of nuclei N, at time t, which is an exponential function in time given by

$$N(t) = N_0 \exp^{-\lambda t} \tag{2.2}$$

where N_0 is the number of nuclei at time t=0. Eq. 2.2 is the law of radioactive decay.

Radioactive decay can also be measured in terms of the half-life. An isotope's half-life is the time required for the number of atoms in a radioactive isotope to decay into half its initial value. Fig. 2.1 shows a theoretical graph of the number of nuclei present as a function of time.

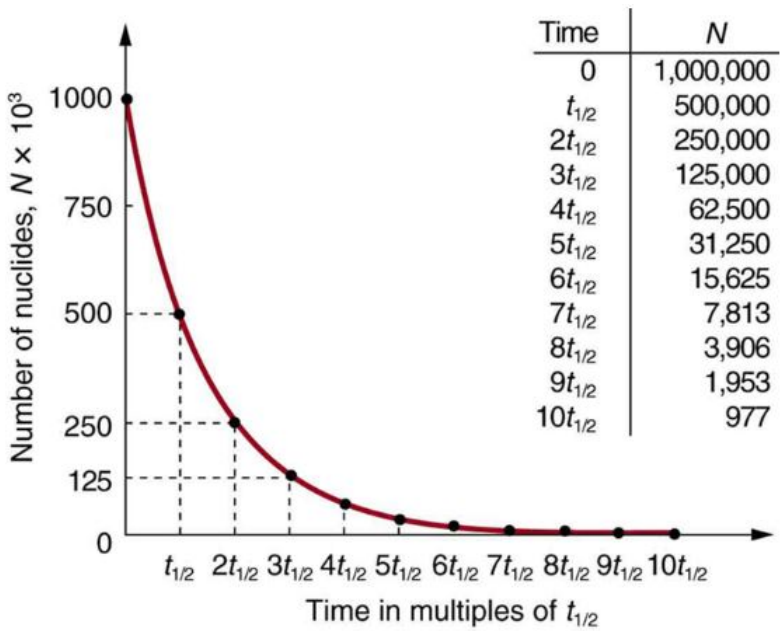

Figure 2.1: Decay rate of a nuclei as a function of its half-life. Figure from Ref. [18].

As shown in Fig. 2.1, the number of nuclei that has not yet decayed diminishes with the number of half-life's that passes. Depending on the decay mode and the relative competition between available decay modes, half-life's can range from approximately 10^{-15} seconds to many times the age of the universe (double β decay has half-life's on the order of 10^{24} years or more). The relationship between half-life and the decay constant λ, is given by

$$T_{1/2} = \frac{\ln 2}{\lambda} \tag{2.3}$$

Another common way to refer to radioactive decay is using activity, which is the disintegration per second of an unstable nuclei. The activity does not depend on the type of decay, but it depends on the number of decays per second. The units are given by:

- Becquerel : 1Bq = 1 disintegration per second.
- Curie : 1Ci = 3.7×10^{10} Bq.
- Rutherford : 10^6 nuclei decays per second.

Activity is just the rate of decay, Eq. 2.1 can be combined with the radioactive decay law to express the activity as

$$A(t) = \lambda N(t) = A_0 \exp^{-\lambda t} \tag{2.4}$$

Activity is proportional to the number of radioactive nuclei and inversely proportional to the half-life.

2.2 β decay

β decay occurs when a neutron transforms into a proton or vice-verse. During this process the mass number remains unchanged but the atomic number changes. There are three distinct β decay

processes called β^+, β^- and Electron Capture (EC). In general, these three processes transmute more exotic parent nuclei to less exotic daughter nuclei.

2.2.1 β^+ decay

In β^+ decay, a proton-rich nucleus converts a proton into a neutron by emitting a positron (β^+) and an electron neutrino (ν_e) [19]:

$$ {}^{A}_{Z}\mathrm{X}_{N} \rightarrow {}^{A}_{Z-1}\mathrm{Y}_{N+1} + \beta^+ + \nu_e + Q_{\beta^+} \tag{2.5} $$

The Q_{β^+} energy value of this reaction is given by

$$ Q_{\beta^+} = [M(A,Z) - M(A,Z-1) - 2m_e]c^2 \tag{2.6} $$

where $M(A,Z)$ is the mass of the nucleus with A nucleons and Z protons, m_e is the mass of the electron and c is the speed of light. According to Eq. 2.6, the total energy is shared between the positron, neutrino, and the recoiling daughter nucleus. It also requires that the mass difference between the parent and the daughter nucleus must be greater than $2m_e c^2$ = 1.022 MeV [19] for β^+ decay to occur. Since positron decay requires energy, it cannot occur in an isolated proton because the mass of the neutron is greater than the mass of the proton. Additionally, because the positron does not exist for a long period of time in the presence of matter, it interacts with an electron in its surrounding environment leading to annihilation. The masses of both positron and electron convert to electromagnetic energy forming two 511-keV γ rays in opposite directions [20]. Typical values for Q_{β^+} are $\sim$ 2 MeV - 4 MeV [19].

2.2.2 β^- decay

In β^- decay, a neutron-rich nucleus converts a neutron into proton by emitting an electron (β^-) and an electron antineutrino ($\bar{\nu}_e$) [19]:

$$ {}^{A}_{Z}\mathrm{X}_{N} \rightarrow {}^{A}_{Z+1}\mathrm{Y}_{N-1} + \beta^- + \bar{\nu}_e + Q_{\beta^-} \tag{2.7} $$

The Q_{β^-} energy value of this reaction is given by

$$ Q_{\beta^-} = [M(A,Z) - M(A,Z+1)]c^2 \tag{2.8} $$

The decay energy is shared between the electron, antineutrino and the recoiling daughter nucleus. The antineutrino like the neutrino, has no charge or significant mass, and does not readily interact with matter. Similarly, the total energy released is the difference between the excitation energies of the initial and final states. Typical values for Eq. 2.8 near stability is ~0.5 MeV - 2 MeV [19].

2.2.3 Electron capture

Electron capture is like β^+ decay in the sense that a proton captures an atomic electron, typically from the innermost shell or K shell:

$$ {}^{A}_{Z}\mathrm{X}_{N} + e^- \rightarrow {}^{A}_{Z-1}\mathrm{Y}_{N+1} + \nu_e + Q_{\mathrm{EC}} \tag{2.9} $$

The Q_{EC} energy value is given by,

$$ Q_{\mathrm{EC}} = [M(A,Z) - M(A,Z-1)]c^2 \tag{2.10} $$

After a proton captures an electron, the electron shell is left with a vacancy and the process is accompanied by emission of a neutrino. Electron fill the lower lying shells which leads to emission of X-rays [20]. Depending on the final state of the daughter nucleus and the binding energy, the

neutrino is emitted with precise energy [19], with neutrino getting approximately all of the Q-value [21]. Though it is possible that neutrinos have some mass, it is very small and has a neutral charge. Therefore, the neutrino escapes undetected from most experimental apparatuses due to the low weak interaction cross section; therefore, the identification of electron capture decay must be followed by tracking the secondary emission of X-rays or Auger electrons.

In general, if Q_{EC} < 1.022 MeV ($2m_e$), β^+ is not feasible, only electron capture can occur. If Q_{EC} > 1.022 MeV ($2m_e$), both electron capture and β^+ can occur. If it is a stripped nucleus (no electrons), electron capture is impossible. If Q_{EC} < 1.022 MeV ($2m_e$) and it is a stripped nucleus, the nucleus becomes stable and cannot decay [21].

In the process of β decay, due to the energy taken away by the neutrino, there is a continuous energy distribution for electron or positron, depending on the reaction (Q) energy. This β energy spectrum can be described by Fermi theory of β decay. In Fermi theory

$$\lambda_{if} = \frac{2\pi}{\hbar}|M_{if}|^2\rho_f \tag{2.11}$$

where λ_{if} is the transition probability, $|M_{if}|$ is the matrix element for the reaction and ρ_f is the density of final states [22].

2.3 β-decay selection rules

Angular momentum and parity conservation has to be satisfied for a β-decay transition to take place. This gives rise to selection rules that determine whether a particular transition between an initial and final state, both with specified spin and parity, is allowed, and, if so, what mode of decay is likely [23]. The two emitted particles, an electron and a neutrino, have a spin of 1/2 and carry orbital angular momentum. The orientation of electron and neutrino plays an important role in

the selection rules. If the spin of the two particles are antiparallel (↑↓), the coupled total spin is S_β=0. This system undergoes a Fermi decay. Whereas, when the two emitted particles are aligned parallel (↑↑ or ↓↓), S_β=1. This is called a Gamow-Teller decay.

The rules for addition of angular momentum vectors implies that

$$|j_{\mathrm{N1}} - j_{\mathrm{e}\bar{\nu}}| \leq j_{\mathrm{N2}} \leq j_{\mathrm{N1}} + j_{\mathrm{e}\bar{\nu}} \tag{2.12}$$

where j_{N1} is the nucleus spin before decay, j_{N2} is the nucleus spin after decay and $j_{\mathrm{e}\bar{\nu}}$ is the combined angular momentum of electron and antineutrino [25].

From Table. 2.1, allowed β decay requires that both electron and neutrino carry no orbital angular momentum ($\Delta l = 0$), and has no change in nuclear parity ($\Delta\pi = 0$). In allowed Fermi decay, there is no change in parity and orbital angular momentum and ΔJ = 0.

In an allowed Gamow-Teller transition, the electron and neutrino carry off a unit of angular momentum. Thus,

$$\bar{j}_{\mathrm{N1}} = \bar{j}_{\mathrm{N2}} + 1 \tag{2.13}$$

Table 2.1: β decay selection rules for allowed and forbidden transitions. Table from Ref. [24].

Transition type	$\Delta\pi$	Δl	Δ J	log ft
Superallowed	No	0	0	2.9 - 3.7
Allowed	No	0	0,1	4.4 - 6.0
First forbidden	Yes	1	0, 1, 2	6 - 10
Second forbidden	No	2	1, 2, 3	10 - 13
Third forbidden	Yes	3	2, 3, 4	$\geq$ 15

$$| \bar{J}_{N2} - 1 | \geq J_{N1} \geq | \bar{J}_{N2} + 1 | \quad \longrightarrow \quad \Delta J = 0, 1 \tag{2.14}$$

Similarly, there is no change in parity between final and initial state. The majority of transitions are mixed Fermi and Gamow-Teller decays, since $\Delta J = 0$ is allowed in both Fermi and Gamow Teller allowed transition. In the special case when there is a transition from a spin 0^+ state to spin 0^+ state ($J_{N1} = J_{N2} = 0$), only Fermi decay is possible and it is called a "superallowed" β decay [25]. The ground state of the nucleus of interest, ^{34}Cl, follows a supperallowed β decay into the ground state of ^{34}S.

Allowed β decay is prohibited when the initial and final states have opposite parities. However, such decays can occur with less probability compared to allowed β decay. These are called forbidden transition type ($\Delta l \geq 0$) [19]. The degree of forbiddingness is dependent on Δl. Decays of Δl=1 are called first forbidden decays, second forbidden decays has Δl=2 [25]. Table. 2.1 summarizes the selection rules for forbidden and allowed β decay transitions.

The $\log ft$ value, also termed the comparative half-life, is a method for comparing the β decay probabilities in different nuclei. The $\log ft$ value can also represent differences between the final and initial state. Approximate values of $\log f_{\beta^-}$ can be calculated from

$$\log f_{\beta^-} = 4.0 \log E_{\max} + 0.78 + 0.02Z - 0.005(Z-1) log E_{\max} \tag{2.15}$$

where $E_{\max}$ is the energy difference in MeV of the mother and daughter final state in atomic number Z of the β daughter [26]. The t in $\log ft$ is the partial half life for the decay to a specific state in the daughter nucleus. Therefore, the partial half life for decay populating a specific state i in the daughter is given by [27]

$$T_{1/2}{}^{\text{partial, i}} = \frac{T_{1/2}{}^{\text{total}}}{BR_{\text{i}}} \tag{2.16}$$

where BR_{i} is the branching ratio to the daughter state i. This ratio defines the constant rate for a particular decay branch to the total set of possible decay branches.

2.4 γ-ray decay

When a nucleus is in an excited state, it can release the energy in the form of electromagnetic radiation (photon) in a process called γ-ray decay. This energy ranges from keV to MeV. During this decay process, there is no change in the proton number and mass number. Most β decays are accompanied by a γ ray because the daughter nucleus is left in an excited state. The level schemes and interconnecting transitions of a radionuclide can be identified by using γ-ray spectroscopy.

Similar to a β decay, the conservation of angular momentum has to be taken into consideration in a γ-ray decay process. The initial and final states have a definite angular momentum and parity. Thus, the angular momentum (L) carried by the photon ranges from

$$|(I_{\mathrm{i}} - I_{\mathrm{f}})|\hbar \leq L \leq (I_{\mathrm{i}} + I_{\mathrm{f}})\hbar \quad \rightarrow \quad L = l\hbar \quad \rightarrow \quad l \geq 1 \tag{2.17}$$

where I_{i} and I_{f} are initial and final nuclear spins respectively [19].

In addition to a change in angular momentum, a change in parity between the initial and final states will be associated with a γ-ray transition. For an electric type transition the change in parity is

$$\Delta\pi = (-1)^{l} \tag{2.18}$$

while for a magnetic transition the change in parity is

$$\Delta\pi = (-1)^{l-1} \tag{2.19}$$

While γ rays have an intrinsic spin of one ($\Delta l \geq 1$), some transitions are forbidden ($\Delta l = 0$) like the decay from $0^+ \rightarrow 0^+$.

2.5 γ-ray interaction with matter

A study of interaction of γ rays with matter is necessary to understand what reactions occur in a detector after a decay. There are 3 major types of γ-ray interactions with matter; namely the photoelectric absorption, Compton scattering and pair production.

2.5.1 Photoelectric absorption

The photoelectric absorption involves the interaction of a γ ray with an inner shell electron. The γ ray interacts with the electron in such a way that all its energy is transferred to the electron, and thus the γ-ray energy is fully absorbed. The majority of the γ-ray energy is transfered to the freed electron as kinetic energy while some is used to overcome the binding energy of the electron. The energy of the released photoelectron E_e is given by

$$E_\mathrm{e} = E_\gamma - E_\mathrm{b} \tag{2.20}$$

where E_γ is γ-ray energy and E_b is electron binding energy. A small amount of recoil energy remains with the atom to conserve momentum. In a radiation detector, photoelectric absorption results in a full energy peak because the γ ray gives up all its energy [28].

The probability of photoelectric absorption depends on the atomic number of the atom, electron binding energy, and the γ-ray energy. The more tightly bound the electron, the higher the proba-

bility. Therefore, the K-shell electrons are mostly affected. The probability is given approximately by

$$\tau \sim \frac{Z^4}{E^3} \tag{2.21}$$

where τ is the photoelectric mass attenuation coefficient [28].

2.5.2 Compton scattering

A γ-ray photon can also interact by losing part of its energy to an electron, with the remainder of its energy emitted as a new lower energy photon. To absorb recoil energy, conservation of momentum and energy allows only a partial transfer when the electron is not tightly bound enough. The kinetic energy of the electron is given as:

$$E_{\mathrm{e}} = E_\gamma - E' \tag{2.22}$$

where E_{e} is the scattered electron energy, E_γ is the incident γ-ray energy, and E' is the scattered γ-ray energy [28]. The scattered γ-ray energy can be written as function of scattering angle and incident γ-ray energy as

$$E'_\gamma = \frac{E_\gamma}{1 + (1 - \cos\theta)\frac{E_\gamma}{m_0 c^2}} \tag{2.23}$$

where $m_0\mathrm{c}^2$ is the electron rest mass (511 keV) and θ is the angle between incident and scattered γ rays.

Fig. 2.2 shows Compton-scattered electron energies as a function of scattering angle and γ ray energy. The sharp discontinuity corresponds to the maximum energy that can be transfered in a single scattering. In a detector, the detector medium stops the scattered electron and the detector produces an output pulse that is proportional to the energy lost by the incident γ ray [28].

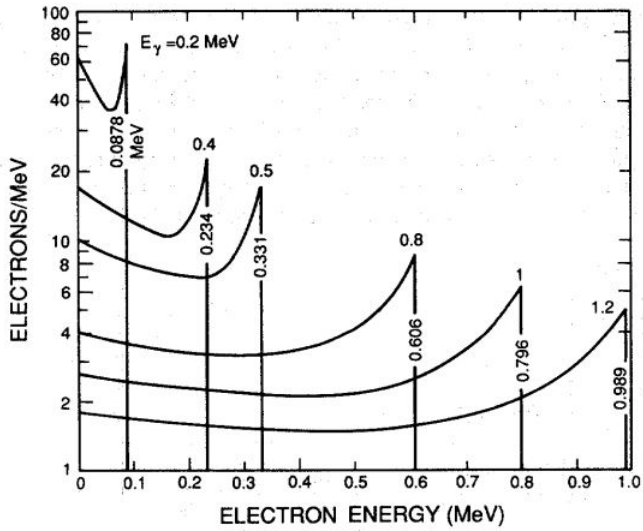

Figure 2.2: Compton-scattered electron energy as a function of scattering angle for several γ-ray energy. Figure from Ref. [28].

2.5.3 Pair production

Pair production is a process by which a photon is converted to an electron-positron pair. This event converts energy into mass using Einstein's relation ($E = mc^2$) because the photon has no rest mass. Any γ ray totaling at least 1.022 MeV (two electron rest masses) can appear as the kinetic energy of the pair and the recoil emitting nucleus, with the probability for pair production increasing significantly above 1.1 MeV as shown in Fig. 2.3.

After the photon conversion, the positron combines with a free electron and both particles annihilate. The entire mass of these two particles is then converted into two γ-ray energies of 0.511 MeV each, and these γ rays may or may not escape the detector. If one or both of these two γ rays escapes the detector, given enough statistics, one can see single and double escape peaks in the energy spectrum at 0.511 MeV and 1.022 MeV below the photopeak, respectively.

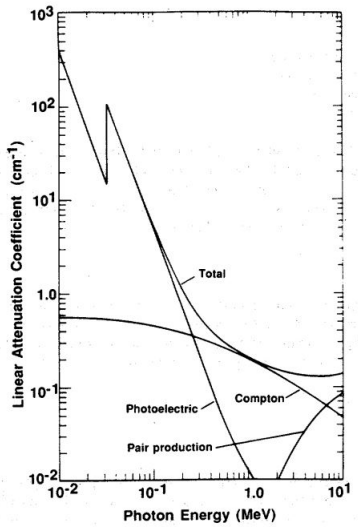

Figure 2.3: Linear attenuation coefficient of NaI showing contributions from photoelectric absorption, Compton scattering and pair production. Figure from Ref. [28].

Pair production is impossible for γ-ray energies less than 1.022 MeV. The probability of pair production is approximately proportional to the square of the atomic number [28].

2.6 Internal conversion

Internal conversion occurs when an excited nucleus interacts electromagnetically with an orbital electron, and ejects it [8]. The vacancy created by the ejected electron is filled by an orbital electron, which results in X-ray or Auger electron emission. The high speed electron should not be confused with the β particle because the electron is not created during the decay process, but is a preexisting atomic electron [29]. The kinetic energy of the emitted electron is given as

$$E_{\mathrm{IC}} = E_{\mathrm{transition}} - E_{\mathrm{electron\ binding\ energy}} \tag{2.24}$$

where $E_{\mathrm{transition}} = E_{\mathrm{i}} - E_{\mathrm{f}}$ is the energy difference between the initial and final state [8].

This mode of decay also occurs and competes with γ-ray decay as a deexcitation process in unstable nuclei. Due to this, many radioactive nuclei could emit both γ rays and internal conversion electrons. The degree to which this occurs is expressed as the total internal conversion coefficient (α), which is the ratio of the rate of emission of internal conversion electrons to the rate of emission of γ rays:

$$\alpha = \frac{N_e}{N_\gamma} \tag{2.25}$$

where N_e and N_γ are the number of internal conversion electrons and γ-ray photons, respectively, in each time interval for a given energy decay transition. The internal conversion coefficient can vary between 0 and ∞ [29].

There is a special case of internal conversion between 0^+ states called an E0 transition. In such transitions, γ rays cannot be emitted as explained in Sec. 2.4, but a transition can proceed through internal conversion [29].

2.7 Bateman equations

The first order differential equations used in describing activities in a decay chain, based on the initial abundance and decay rates can be described by the Bateman equations [30]. The first, or parent, decay has its rate of decay governed by its decay constant. The second, or daughter decay, has to then account for the growth in activity due to the decay of the parent as well as its own decay due to its decay constant. Similar arguments are made for each subsequent member for the decay chain. Therefore, for a series of radioactive decays of n-nuclide's in a linear chain, the Bateman equations are derived as

$$\frac{dN_1}{dt} = -\lambda_1 N_1 \tag{2.26}$$

$$\frac{dN_{\mathrm{i}}}{dt} = \lambda_{\mathrm{i\text{-}1}} N_{\mathrm{i\text{-}1}} - \lambda_{\mathrm{i}} N_{\mathrm{i}}; (i = 2...n) \tag{2.27}$$

where λ_{i} is the decay constant of the i^{th} nuclide. Taking into account that there are no concentrations in all daughter nuclei at time zero, the initial conditions are specified as

$$N_1(0) \neq 0; N_{\mathrm{i}}(0) = 0; i > 1 \tag{2.28}$$

Therefore, the n^{th} nuclide concentration after a time t is given by the Bateman equation

$$N_{\mathrm{n}}(t) = \frac{N_1(0)}{\lambda_{\mathrm{n}}} \sum_{i=1}^{n} \lambda_{\mathrm{i}} \alpha_{\mathrm{i}} \exp[-\lambda_{\mathrm{i}} t] \tag{2.29}$$

where

$$\alpha_{\mathrm{i}} = \prod_{j=1; j \neq i}^{n} \frac{\lambda_{\mathrm{j}}}{(\lambda_{\mathrm{j}} - \lambda_{\mathrm{i}})} \tag{2.30}$$

[30]. Eq. 2.30 can only be calculated if all decay constants are different, otherwise it goes to infinity. The presence of infinity in the sum means it will not converge [30].

While the Bateman equations will be used in later analysis, the results of this subsequent analysis are likely to be less precise than the results presented in this work due to needing to develop a time binning for the fitting of our results, thereby reducing the count in our analyzed photopeaks. The Bateman equation application to the data is left as a future project and will be briefly described in Chapter 5.

CHAPTER III

FACILITIES AND INFRASTRUCTURE FOR PERFORMING E16032A EXPERIMENT

In this chapter, the experiment 16032A which was carried out at the National Superconducting Cyclotron Laboratory (NSCL) is described. Sec. 3.1 begins with a general description of the NSCL at Michigan State University (MSU). A description of the cyclotrons working principle is given in Sec. 3.2. Sec. 3.3 describes the primary beam and reaction target used for isotope production. A detailed description of the A1900 fragment separator is introduced in Sec. 3.4.

3.1 National Superconducting Cyclotron Laboratory (NSCL)

The experiment 16032A was carried out at the National Superconducting Cyclotron Laboratory (NSCL) at Michigan State University (MSU). The facility produces rare isotope beams at a wide range of energies through projectile fragmentation [31, 32]. Sec. 3.3.1 discusses projectile fragmentation in some detail. The NSCL utilizes two superconducting cyclotrons coupled together (the K500 and the K1200), which also gives it the common name of the Coupled Cyclotron Facility (CCF). A diverse array of experimental devices are available for conducting experiments [33].

In this experiment, a ^{34}Cl beam was produced using an Ar^{16+} primary beam at 150 MeV/u via fragmentation in an ~1.2 mm thick Be target. The ^{34}Cl was identified through its Time of Flight (ToF) between a scintillator at the image 2 (i2) focal plane of the A1900 fragment separator and

a 65 μm Silicon PIN diode detector positioned near the experimental end station, and the energy loss measured using the same Si PIN detector.

3.2 Cyclotrons

A cyclotron is a device that accelerates particles to high velocities using a magnetic field and a time varying electric field. The cyclotron was originally developed by Ernest Lawrence in 1930. Cyclotrons are generally composed of "dees", which is a set of "D" shaped hollow conductors. A image of a two dee cyclotron is shown in Fig. 3.1.

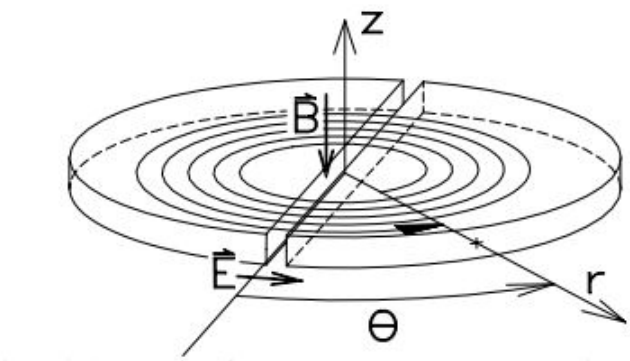

Figure 3.1: A two dee cyclotron. Figure from Ref. [34].

To accelerate a particle, the cyclotron uses hollow metallic electrodes (dees) to which a time varying radiofrequency (RF) electric potential is applied resulting in an electric field between the dees in the gap. The time varying electric field accelerates the particles in the azimuthal θ direction and the DC magnetic field bends the beam particle around a closed orbit about the $\hat{z}$ direction. The potential changes every half a cycle as the particles move, but it is constant with respect to each dee. Thus, the electric field inside cavity of the dee remains zero. This then requires the frequency

of the voltage source to be equal to the cyclotron frequency of the particle [34] as described in the next section.

3.2.1 Cyclotron radiofrequency (RF)

Acceleration of ions is dependent on the RF potential applied to the dees [35] as mentioned in Sec. 3.2. To derive an equation for the cyclotron frequency by looking at the interaction of a charge particle with a magnetic field, the force on a charged particle as a result of circular motion is considered and given by

$$\vec{F}_{\text{mag}} = q\,\vec{v}\times\vec{B} \tag{3.1}$$

where $\vec{F}_{\text{mag}}$ is the magnetic force acting on a charged particle with charge q moving inside a magnetic field B. The Newton's second law statement that describes the centripetal force that makes the particle move in a curved path is given by

$$\vec{F}_{\text{cent}} = -(\frac{mv^2}{r})\hat{n} \tag{3.2}$$

where $\vec{F}_{\text{cent}}$ is the centripetal force, m is mass of the particle and n is perpendicular to the trajectory [36]. The RF frequency is based on Eq. 3.1 and Eq. 3.2 where $\vec{v}$ and $\vec{B}$ must be perpendicular to each other. Equating Eq. 3.1 to Eq. 3.2 gives

$$\frac{q|B|}{m} = \frac{v}{r} = \omega_{\text{RF}} \tag{3.3}$$

Eq. 3.3 yields the magnetic field for closed orbits, where ω_{RF} is constant for a given particle. A measure of the particle coupling strength to the magnetic field can be given by the magnetic

rigidity, B_ρ, which is the magnet bending strength for a given radius and energy [37]. It is given by:

$$B_\rho = \frac{p}{q} = \frac{mv}{q} \tag{3.4}$$

where p is the momentum, q is the charge, v is the velocity, and m is the mass . The unit for magnetic rigidity is Tesla-meters [37].

3.2.2 Coupled Cyclotron Facility

In 1999, the NSCL upgraded to the Coupled Cyclotron Facility (CCF), see Fig. 3.2, to help provide substantial beam intensity for ions and increased energies. Before the coupling of the cyclotrons, the K500 and K1200 individually accelerated heavy-ion beams. The new facility couples the K500 and K1200 to produce ion beams from Hydrogen to Uranium ranging from 200 MeV/u to 90 MeV/u [38]. The "K" in K500 and K1200 indicates the maximum kinetic energy that a Hydrogen (proton) beam can be accelerated to in MeV. The "K" comes from multi-particle cyclotrons where the energy from an ion of charge Q and mass m_o is given non-relativistically by [39]

$$E = \frac{KQ^2}{A} \tag{3.5}$$

As shown in Fig. 3.2, the CCF houses both the K500 and K1200 cyclotrons. The basic requirements of the cyclotrons are to produce and transport rare isotope beams between two cyclotrons and match six-dimensional phase space to ensure efficient injection into the K1200 cyclotron [31, 40]. The production of rare isotopes initially begins with a stable beam (like ^{40}Ca) which is accelerated by the K500 cyclotron to velocities of ~0.2c.

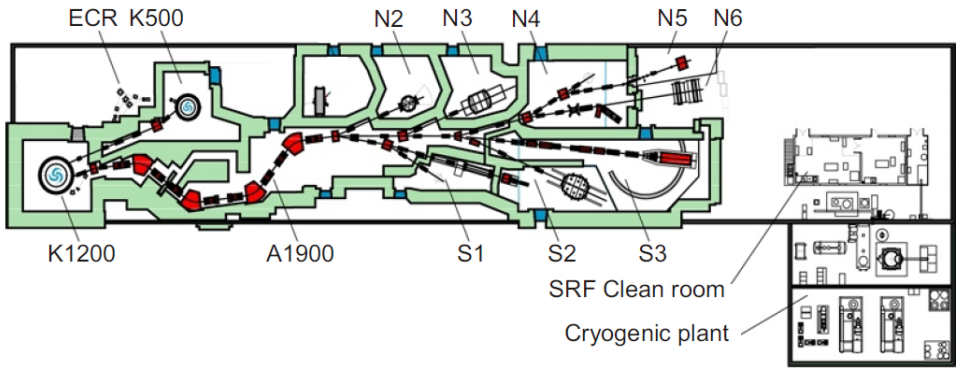

Figure 3.2: Layout of the coupled cyclotron facility consisting of K500 and K1200 cyclotrons, the A1900 fragment separator and the experimental vaults N2-N6 and S1-S3. Image from Ref. [40].

The high energy beam then passes through the K1200 cyclotron carbon stripper foil thereby removing electrons and increasing its charge state to maximize its energy in the final stage of acceleration. The primary beam strikes a production target, thereby resulting in the creation of several isotope species. Before the rare isotopes are delivered into any of the 8 experimental vaults (labeled S1-S3 and N2-N6 in Fig. 3.2), the A1900 separates incoming isotopes according to magnetic rigidity. The A1900 fragment separator will be discussed in detail in Sec. 3.4.

3.3 Primary beam and reaction target

In the experiment 16032A carried out at NSCL, the ion of interest ^{34}Cl, was created with a primary beam of Ar^{16+} at 150 MeV/u. The Ar^{16+} beam was initially accelerated to 13 MeV/u in the K500 cyclotron with a charge state of $+7e$ and was further accelerated to 150 MeV/u in the K1200 cyclotron with a charge state of $+18e$. The Ar^{16+} beam was then fragmented by an ~1.2mm

Be thick target. Beryllium is a commonly used production target due to its relatively large nuclear number density [40].

3.3.1 Fragmentation process for producing exotic nuclei with large N/Z ratio

Exotic nuclei are short-lived nuclei that have large proton/neutron ratios as compared to the stable nuclei found in nature. Exotic nuclei are difficult to produce and study because of the simultaneous production of contaminant species and low production cross sections [41].

Fig. 3.3 shows the layout of the nuclear landscape in which the proton and neutron numbers are drawn on the vertical and horizontal axis, respectively. The blue squares indicate stable isotopes which form our universe while the yellow squares indicate the exotic nuclei which have been observed experimentally. For the medium-mass nuclei below Z=20 and N=28, the magics numbers are shown at 2, 8, 20 and 28. The most predominant ways of producing exotic nuclei are Isotope Separation On Line (ISOL) and in-flight separation using heavier ions (fragmentation technique) [42]. The latter will be discussed because of its relevance to the experiment 16032A.

In the fragmentation technique, a high energy beam is fragmented by hitting a target nucleus which is typically ^{9}Be. The production of exotic nuclei depends on its distance from the stability line. The ion's Coulomb deflection and nuclear recoil are small so that the large initial velocity can focus all the products into a narrow cone. The mass, charge, and velocity distributions of the products can be described by two models; namely the microscopic nucleon-nucleon scattering model and the macroscopic abrasion framework [43].

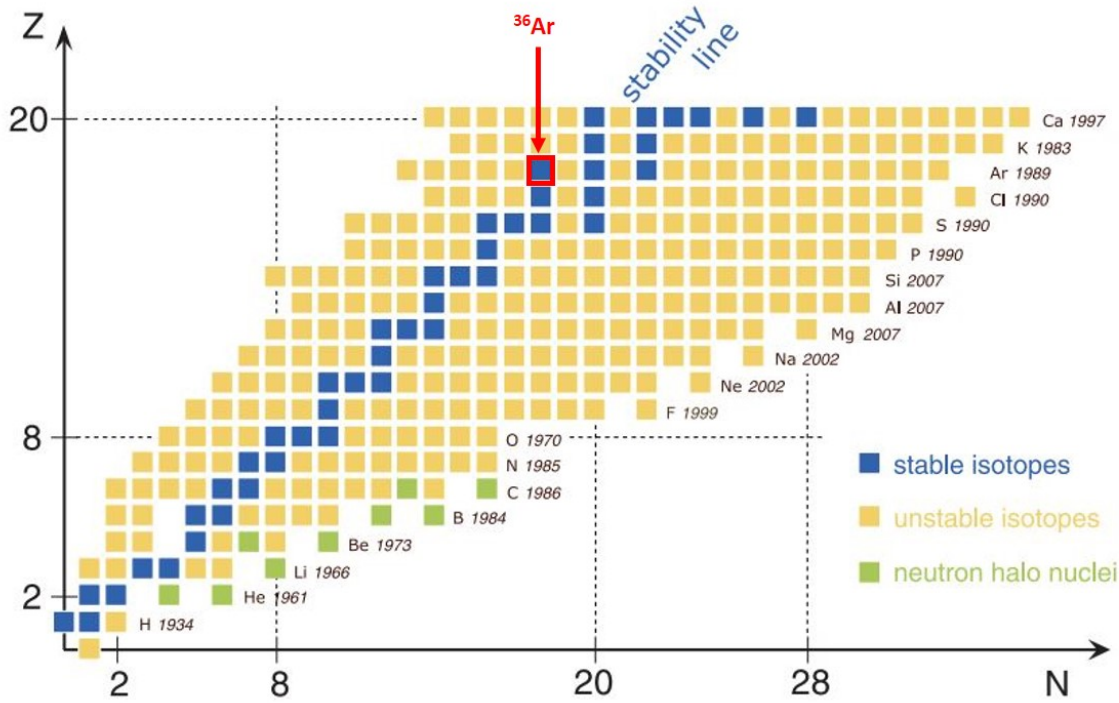

Figure 3.3: Atomic nuclei landscape indicating stable and exotic nuclei. Figure adapted from Ref. [44].

The microscopic nucleon-nucleon scattering model is best utilized for beam energies below 100 MeV/u. The microscopic nucleon-nucleon scattering model predicts many features of the collision such as the total elastic cross-section and the mean free path of individual nucleons in the target. Conversely, in the macroscopic abrasion framework, the target causes shearing off of particles from the projectile nucleus, leaving the rest of the projectile to move at nearly the initial beam velocity, carrying along some excitation energy and small downshift in velocity [43].

In the cases where the masses of the fragments are close to but smaller than that of the initial nucleus, the fragment is maximized and the mass fragments follow an exponential decrease with

respect to the projectile mass number. The isotonic distribution produces neutron numbers that are much lower than stability. Also, the isotonic distribution is almost Gaussian. Only lower mass fragments are expected to be produced. For example, when proton-rich nuclei are close to stability, they are best produced with the heavier N~Z projectiles. On the other hand, neutron-rich nuclei are produced with neutron-rich beam [43].

At the NSCL, after fragmentation, the nuclei of interest are then separated using the A1900 fragment separator.

3.4 A1900 fragment separator

The A1900 fragment separator is a high acceptance magnetic fragment separator that utilizes four 45° superconducting, iron-dominated dipole magnets, labeled D1-D4 in Fig. 3.4, with a 3m radius and 24 superconducting large-bore quadrapole magnets housed in 8 cryostat used to focus the beam [40, 45].

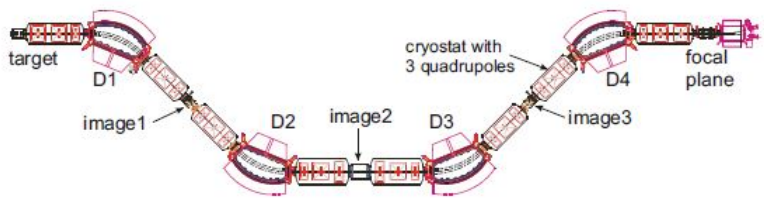

Figure 3.4: Detailed picture of A1900 showing superconducting dipole magnet D1-D4 and 24 quadrupole magnets housed in 8 cryostats. Figure from Ref. [40].

The quadrupoles focus the beam in one direction, either x or y, therefore several quadrupoles are used [45]. Table 3.1 shows the fundamental properties of the A1900 fragment separator.

Table 3.1: Fundamental properties of A1900. Table from Ref. [40].

Parameter	A1900
Momentum acceptance (%)	5
Maximum rigidity (Tm)	6
Resolving power	2915
Dispersion ($mm/\%$)	59.5
Solid angle [msr]	8

Fig. 3.4 gives a detailed pictorial description of the A1900 fragment separator. The fragments are initially produced after a primary beam hits a target. The mixture of primary and secondary beams ions is then bent by the D1 and D2 dipoles to separate a secondary beam according to its magnetic rigidity, B_ρ, given by Eq. 3.4. The beam components are separated by the dipoles by choosing particles within a narrow range of magnetic rigidity [46].

Following the fragmentation filtering from D1 and D2, the ions go into image2 (Fig. 3.5). Image2 is positioned halfway along the A1900 fragment separator where the beam is focused so that a narrow cut can be made on the magnetic rigidity to select a subset of the fragmentation particles in the beam. As the beam passes through image2, it becomes separated spatially based on its B_ρ value.

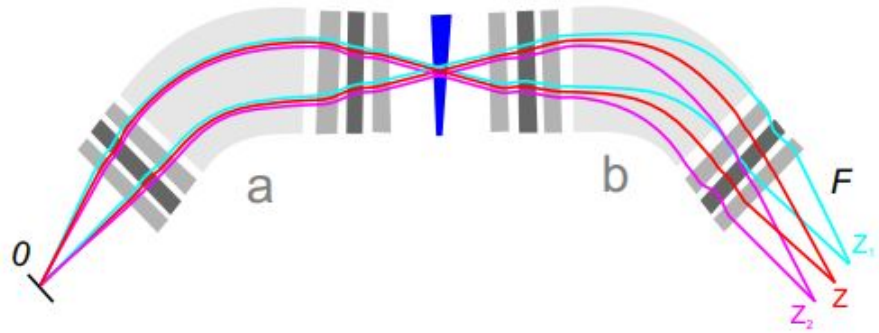

Figure 3.5: Wedge degrader shown in image2. A degrader slows down the beam particles depending on their charge and velocity differences. At the second stage, the different isotopes are now separated. Figure from Ref. [47].

An Al degrader is placed at the image2 to assist with desired isotope selection. The Al degrader is added as a way to differentially change the velocity (rigidity) so that a second selection at the focal plane gives further separation. As shown in Fig. 3.5, in order to keep the achromatic (colorless) condition unchanged for the isotope of interest, the degrader is made to be wedged shape. The wedge shape is necessary to make the beam nearly monoenergetic. The degrader is wedge shape because the energy loss in the degrader depends on the particle velocity. The wedge is thicker at the higher velocity end while it is thinner at the lower velocity end [46, 47]. The degrader's energy loss is proportional to Z^2/v^2, meaning energy loss depends on the different number of protons in the ions. After the degrader, a second B_ρ selection occurs on ions with different Z but similar mass-charge ratios. Then a slit with a 5% maximum acceptance is located after the degrader to control the overall momentum acceptance $\frac{\delta p}{p}$ [32]. The second pair of dipoles, D3 and D4, compensate for the dispersion from the first pair of dipoles, as well as the magnification from selecting a momentum cut. The choice of primary beam, target, degrader material, degrader thickness, and apertures in the fragment separators are parameters adjusted to control the intensity and purity of the rare isotope beam [48].

3.5 Ion implantation into a $CeBr_3$ scintillator

The $CeBr_3$ implantation detector system is a fast scintillator detector with pixelated output used in the experiment 16032A. It is capable of detecting high energy fragmentation ions, enabling correlation of the implanted ions to subsequent decays within the detector, and provides sub-nanosecond time resolution. The Position Sensitive Photo-Multiplier Tube (PSPMT) is coupled to the thick $CeBr_3$ implantation detector (49mm $\times$ 49mm $\times$ 3mm). The implantation scintillator

system consists of a 16×16 pixelated PSPMT which has 256 anodes used to determine the interaction position and timing between pixels, and a single dynode used for full-energy determination and timing information.

3.6 Segmented Germanium Array (SeGA) detector

The Segmented Germanium Array (SeGA) detector is primarily used for γ-ray spectroscopy at the NSCL. Its has an excellent energy resolution for γ-ray spectroscopy and it allows for the separation of closely spaced γ-ray energies. The SeGA detector detects a coincident γ ray emission if a β decay populates the daughter nucleus in an excited state. The configuration used for the SeGA is called a "beta-SeGA" configuration which consist of two concentric rings of 8 detectors that places the $CeBr_3$ detector at the center in order to maximize SeGA detector efficiency. The nominal energy resolution of the SeGA detector, stated in terms of the Full Width at Half Maximum (FWHM), is 0.13% at 662 keV and the nominal efficiency of the array in the "beta SeGA" configuration is 4.48% at 662 keV.

CHAPTER IV

EXPERIMENTAL RESULTS

In this chapter, a complete analysis of the experiment 16032A is presented. The chapter begins with the types of decay, energy levels, decay modes and decay schemes of ^{34}Cl. The following section goes further into determining the number of implanted ^{34m}Cl through data analysis. It then ends on the analysis of implanted ^{34}Cl ions and PID (Particle Identification) plots.

4.1 The decay of ^{34}Cl

Earlier experiments have been performed on ^{34}Cl and a great deal was previously known about this isotope. These studies have been of paramount importance for understanding the evolution of nuclear structure in the ^{34}Cl region. There are two different decay possibilities in ^{34}Cl, namely β decay and internal transition.

The decay scheme shown in Fig. 4.1 represents the β^+ decay at the $J^\pi = 0^+$ ground state of ^{34}Cl, which has a half life of 1.5266(4) s and decays to the $J^\pi = 0^+$ ground state of ^{34}S with a branching ratio of 100%. From Eq. 2.10, the Q value of this decay is 5491.634(43) keV [49, 50].

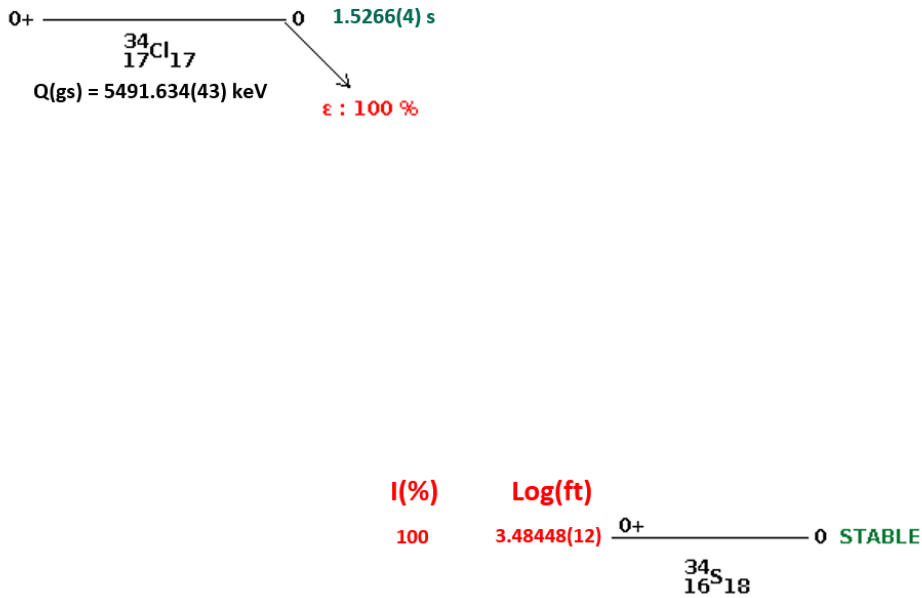

Figure 4.1: Decay scheme of the $J^{\pi} = 0^{+}$ ground state of ^{34}Cl, which has an half life of 1.5266(4) s and decays to the $J^{\pi} = 0^{+}$ ground state of ^{34}S with a branching ratio of 100%. Figure adapted from Ref. [49].

The decay scheme shown in Fig. 4.2 represents the evaluated data pertaining to the decay of the $J^{\pi} = 3^{+}$ isomeric state of ^{34}Cl. This state, ^{34m}Cl (see Fig. 4.2), which has a half-life of 31.99(3) minutes, has a 44.6(6)% probability for an internal transition of E_{γ} = 146 keV to occur and a 55.4(6)% probability for a β^{+} decay to occur. The β^{+} decay results in the following three most intense γ rays in the daughter nucleus, ^{34}S:

- 1176.650(20) keV = $2^{+}_{2} \rightarrow 2^{+}_{1}$
- 2127.499(20) keV = $2^{+}_{1} \rightarrow 0^{+}_{1}$
- 3304.031(20) keV = $2^{+}_{2} \rightarrow 0^{+}_{1}$

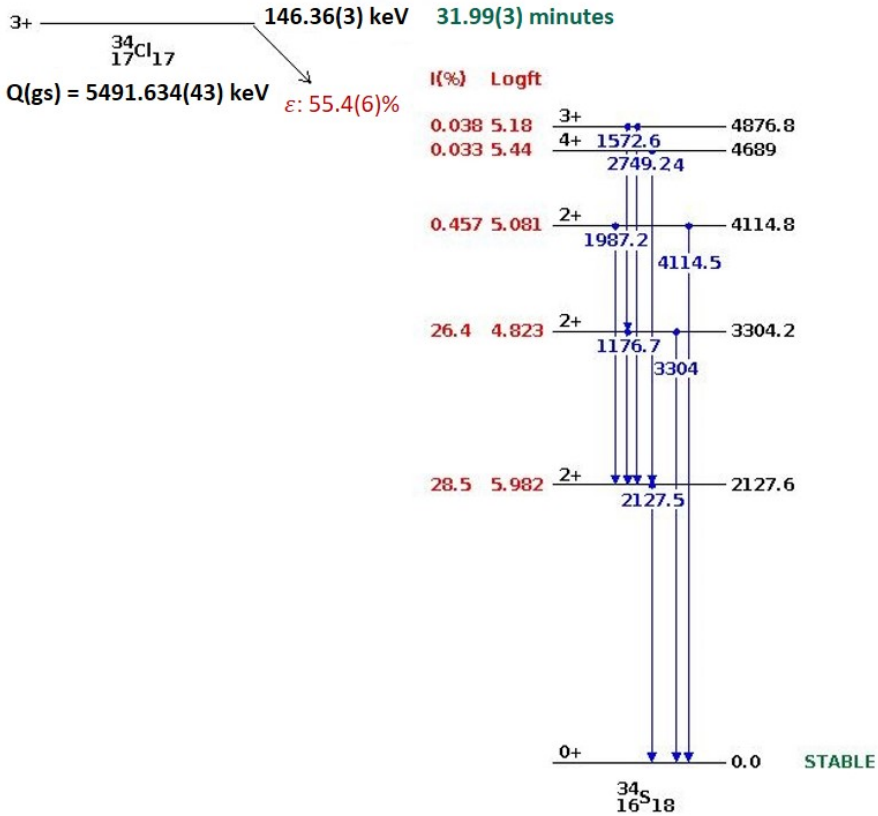

Figure 4.2: Decay scheme of ^{34m}Cl, $J^{\pi} = 3^{+}$, which has an half life of approximately 31.99(3) minutes and decays through internal transition (44.6(6)%) and β^{+} decay (55.4(6)%). The intensity shown is the β^{+} decay feeding intensity for the $J^{\pi} = 3^{+}$ level. Figure from Ref. [49]

These 3 intense γ rays has a known absolute intensities of 14.09(24)%, 42.80(8)% and 12.29(22)% respectively [50]. All other γ rays, such as 1572.57(5) keV, 1987.19(3) keV, e.t.c, have a very small absolute intensity and the discussion on the analysis excludes them from consideration towards the final results [49, 50].

Also, based on the relatively high-density of $CeBr_3$ implantation detector when compared to other common scintillator materials and the ongoing analysis to determining the SeGA absolute efficiency of the 146 keV γ ray energy, the remainder of this report ignores the 146-keV γ ray.

4.2 Determining the amount of ^{34m}Cl in the beam

The following sections will describe efforts taken to determine the overall fraction of ^{34m}Cl in the ^{34}Cl beam delivered to the experimental end station. The beginning of the section discusses ways in which the SeGA detector was calibrated in order to determine the absolute amount of ^{34m}Cl and ^{34}Cl in the beam. The section follows up with the clarification of six beam settings used to select ^{34}Cl ions momentum distribution, branching ratios, and efficiency corrections.

4.2.1 Detection setup characterization

In order to determine the total number of ^{34m}Cl, the absolute number of the γ rays which were emitted by the source is needed. Hence, the number of observed γ rays divide by the absolute efficiency of the detector array is also needed. Therefore, energy and efficiency measurement of the SeGA detectors is crucial, as well as a proper deadtime measurement. To explore ways of maximizing ^{34m}Cl production, 6 different beam settings were utilized and the resultant γ-ray production of the delivered ions were analyzed.

4.2.1.1 SeGA energy calibration

The SeGA detectors shows linear response to incident γ rays between tens of keV and tens of MeV range. Therefore, it is possible to make a linear calibration using some very strong characteristic background γ rays. These γ-ray energies include [51]

- 510.999(15) keV, associated with annihilation of positrons and electrons
- 788.744(8) keV, γ-radiation of ^{138}La found in $LaBr_3$ detectors used in the setup
- 1435.795(10) keV, γ-radiation of ^{138}La found in $LaBr_3$ detectors used in the setup
- 1460.820(5) keV, γ-radiation of ^{40}K from surroundings

When a γ ray hits the detector, after the digitization and evaluation by the pixie-16 module, the channel number of the Multi Channel Analyzer (MCA) storing the amplitude of the incident γ ray is proportional to its energy. Therefore, a linear relation between the incident γ-ray energy and the MCA channel number can be given as:

$$C = aE + b \tag{4.1}$$

where E is the γ ray energy, a is the slope, C is the channel number storing the amplitude of the γ ray in the MCA and b is the intercept. The energy scale calibration for experiment 16032A was set to 1 keV/channel.

Previous experiments calibration parameters for SeGA were initially used in the experiment 16032A SeGA calibration, with the initial assumption that the physical conditions (bias voltage, temperature, e.t.c) for operations on SeGA are the same. Therefore, we write this in the form of

$$C' = a_0E + b_0 \tag{4.2}$$

where C' is the current reading of γ-ray energy. The response of SeGA experiences changes over time because of the fluctuation of vault room temperature. Therefore, a second round of calibration is given by the relation:

$$E = a_1 E' + b_1 \tag{4.3}$$

where E is the desired reading of the γ-ray energy. From Eq. 4.2 and Eq. 4.3:

$$E = a_1 a_0 C + a_1 b_0 + b_1 \tag{4.4}$$

where $a = a_1 a_0$ is the slope and b = $a_1 b_0 + b_1$ is the slope.

4.2.1.2 SeGA Absolute Efficiency Calibration

The thick $CeBr_3$ implantation detector prevents direct measurement of the absolute efficiency because the detector hinders the placement of National Institute of Standard and Technology (NIST) calibrated source at the implant position. This therefore requires simulation of the actual experimental conditions. The absolute efficiency calibration performed on SeGA further requires extraction of relative and absolute γ-ray intensities. Data were taken with a NIST-calibrated Standard Reference Material (SRM) comprised of ^{125}Sb, ^{154}Eu, ^{155}Eu [32] located on the face of the $CeBr_3$ (this gives the best ability to reproduce the effects of the $CeBr_3$ crystal at least on one side of the SeGA array). Since this source is over 20 years old, the ^{125}Sb, which has a half-life of 2.76(25) years, has largely decayed away, leaving only ^{154}Eu and ^{155}Eu for use in the efficiency determination.

A simulation was designed to replicate the material (both sensitive detector and non-sensitive materials) as well as the geometric configuration found in our experimental setup. The simulation was performed with the GEANT4 toolkit for the simulation of the passage of particles through

matter. The isotropic cylindrical volume (button source) for the SRM was reproduced in the simulation to refine the materials present for both the upstream and downstream sides of our SeGA array in the β-SeGA configuration (8 detectors upstream and 8 detectors downstream of the thick $CeBr_3$ implantation scintillator). LISE++ was used [52] to determine the depth profile for the source and implantation data in the $CeBr_3$.

Six beam settings were utilized in the experiment 16032A, so ion implantation had to be carried out for each settings as the implantation profiles and depth distributions informed the creation of the volume source and its positioning inside the $CeBr_3$ detector. Fig. 4.3 - Fig. 4.8 displays the ^{34}Cl ion depth distribution taken for experiment 16032A. A detailed description of the beam settings used is described in Sec. 4.2.2. Fig. 4.3 - Fig. 4.8 were generated using the LISE++ code [32] with parameters set to replicate the experimental beam settings while also illustrating the full 3 mm (3000 μm) thickness of the $CeBr_3$ detector.

The efficiency simulation was run for eleven γ-ray energy values ranging from 100 keV to 4000 keV with the isotropic volume source emitting one million mono-energetic γ rays. The simulated γ-ray results for each beam settings is plotted on a log-log scale as shown in Fig. 4.9.

The simulated log-log scale enabled a sixth order polynomial to be used for interpolation. The log-log fit scale is the best way of describing the simulated γ-ray efficiency for ease of fitting compatibility.

The simulated data points were fit using a linear least-squares fit to the sixth order polynomial function of the form

$$Eff[E_\gamma](\%) = 100 \times 10^{[a(x)^6+b(x)^5+c(x)^4+d(x)^3+e(x)^2+f(x)+g]} \tag{4.5}$$

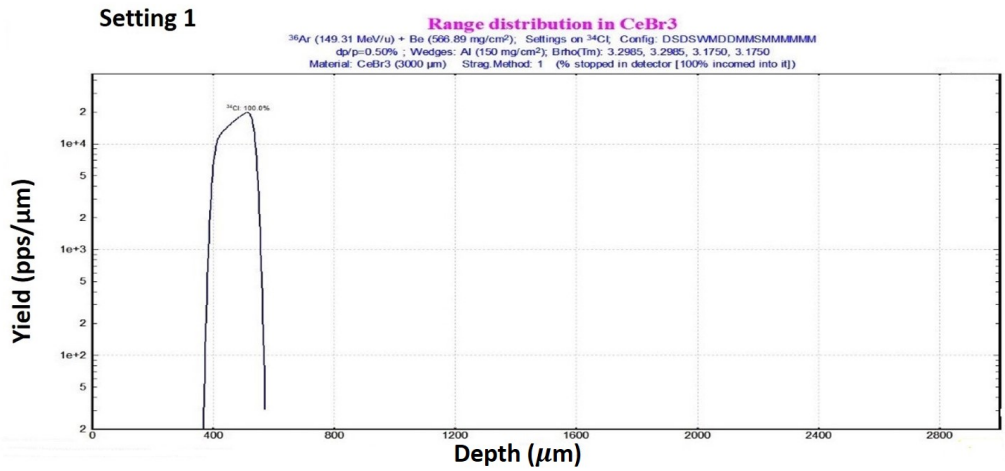

Figure 4.3: Setting 1 ^{34}Cl ion normalized implantation depth distribution inside the $CeBr_3$.

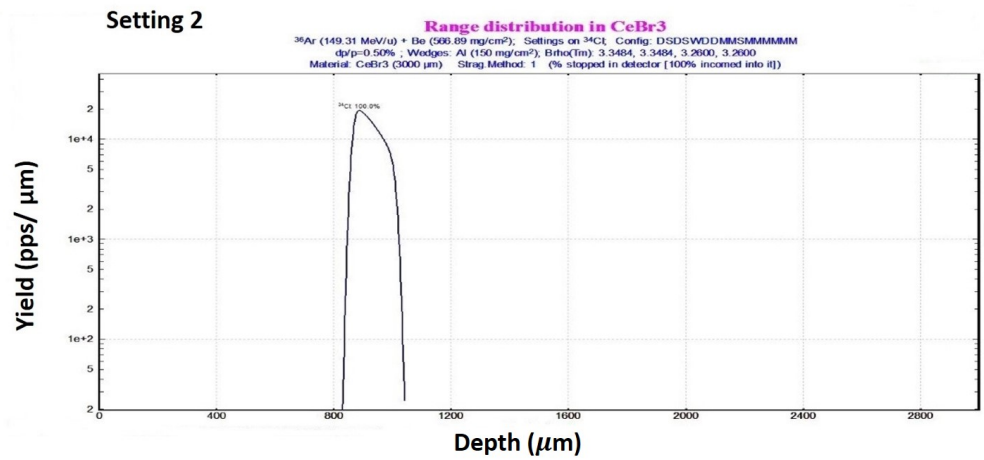

Figure 4.4: Setting 2 ^{34}Cl ion normalized implantation depth distribution inside the $CeBr_3$.

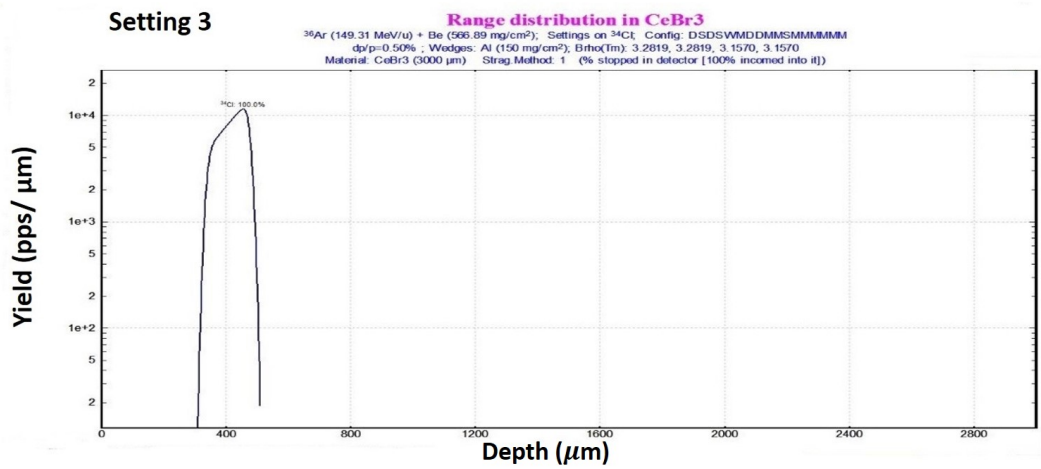

Figure 4.5: Setting 3 ^{34}Cl ion normalized implantation depth distribution inside the $CeBr_3$.

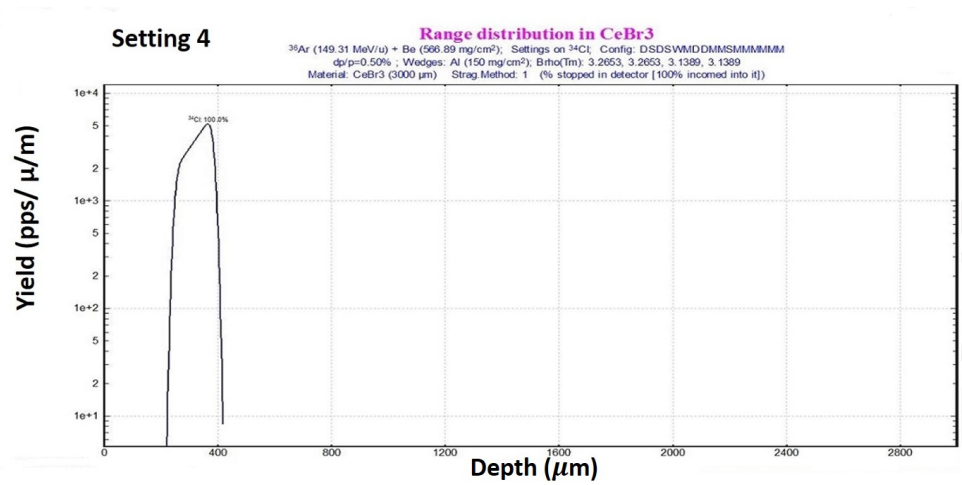

Figure 4.6: Setting 4 ^{34}Cl ion normalized implantation depth distribution inside the $CeBr_3$.

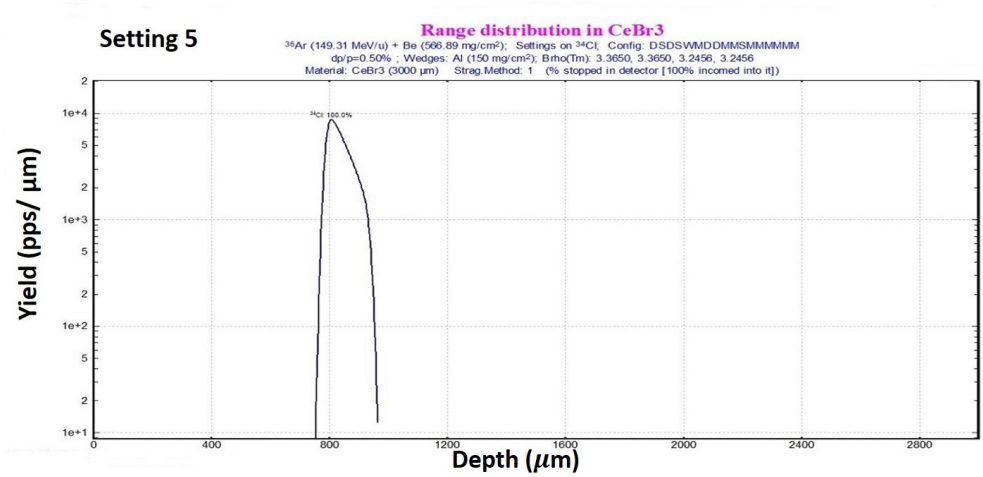

Figure 4.7: Setting 5 ^{34}Cl ion normalized implantation depth distribution inside the $CeBr_3$.

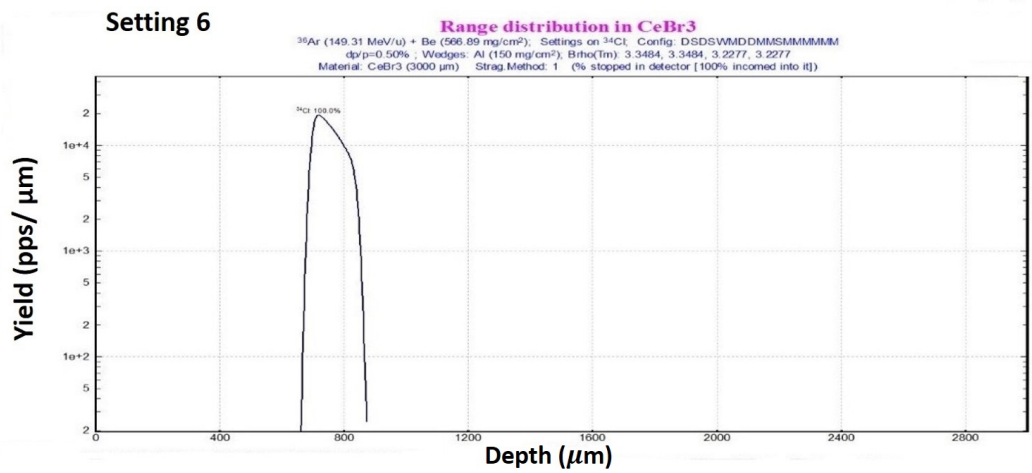

Figure 4.8: Setting 6 ^{34}Cl ion normalized implantation depth distribution inside the $CeBr_3$.

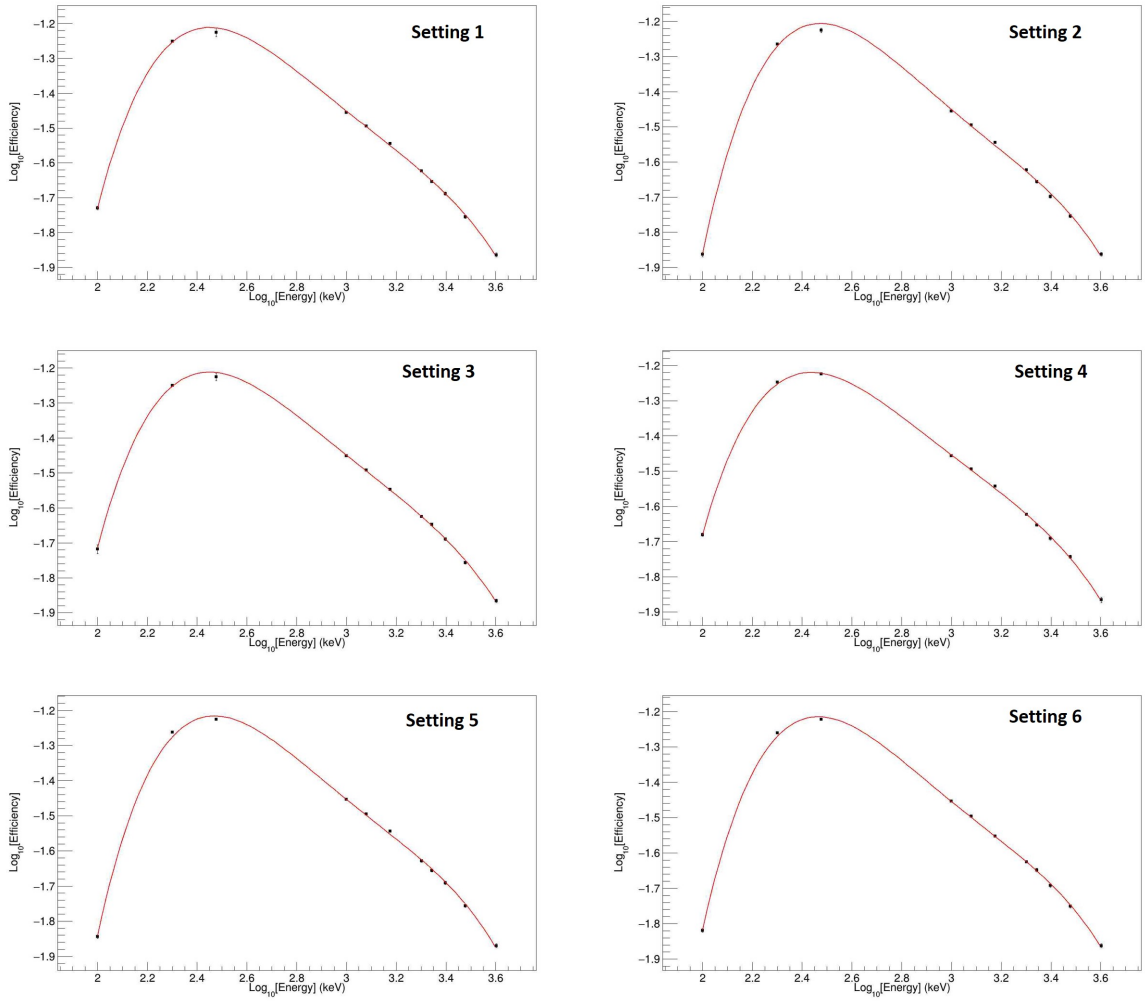

Figure 4.9: Simulated γ-ray efficiency - Setting 1-6

where x=$\log_{10}(E_\gamma)$ and E_γ is the γ-ray energy in keV. The resulting parameter for this six different depth profiles are given in Table 4.1. The absolute efficiencies obtained from these fit curves for the three γ rays of interest could then be used in out analysis.

A 5% uncertainty was assigned to all efficiency calculations across each energy for all the beam settings based on the comparison of the simulation with the SRM data because at lower

Table 4.1: Parameters used in Eq. 4.5 to calculate the γ-ray detector efficiency of SeGA.

Parameter	Setting 1	Setting 2	Setting 3	Setting 4	Setting 5	Setting 6
a	0.082342	0.077462	0.083441	0.083492	0.077335	0.078313
b	-0.078313	-1.358550	-1.398310	-1.397500	-1.357770	-1.363430
c	8.915530	8.927450	8.914120	8.990000	8.920660	8.915310
d	-26.211300	-26.537900	-26.143000	-26.120600	-26.527700	-26.471700
e	30.040000	29.545400	30.106400	30.445800	29.752300	29.882500
f	7.336700	11.758000	6.586340	5.202560	10.867700	10.020500
g	-30.276100	-35.575300	-29.387400	-27.909800	-34.593100	-33.640100

energies, they had the largest uncertainties which is less than 5%. Therefore, a 5% uncertainty was implemented on all parameters as a conservative approach.

4.2.1.3 Deadtime correction

Dead time is the shortest time interval between two pulses, so that both can be recorded as separate pulses [53]. The dead-time correction was determined using internal live-time scalers, as the ratio of accepted triggers to total triggers for each channel of the Digital Data Acquisition System (DDAS) [32]. The count rates for different runs were low enough so that the deadtime correction was not significant.

4.2.2 Beam settings clarification

Four A1900 settings were used to select ^{34}Cl ions from the momentum distribution, with two of the beam settings (Setting 5 and Setting 6) altering the angle of the beam going into the

A1900 fragment separator. The momentum acceptance was 0.5% in all beam settings. The ^{34}Cl momentum distribution settings includes

- 1st slice up: rigidity of the A1900 between the target and wedge is set at 0.75% above "LISE++ optimum"
- 1st slice down: rigidity after target is 0.75% below "LISE++ optimum"
- 2nd slice down: rigidity after target is 1.25% below "LISE++ optimum"
- 3rd slice down: rigidity after target is 1.75% below "LISE++ optimum"

"LISE++ optimum" is the rigidity value that LISE++ predicts for the peak of the fragment's distribution in rigidity. No measurement was taken close to "LISE++ optimum" because the rigidity of the Ar^{16+} primary beam overlapped with the "LISE++ optimum" setting. The angle measurements were made using the 1st slice up setting for the A1900. The angle on the beam was implemented by utilizing a horizontal steering magnet and a horizontal dipole magnet between the K1200 cyclotron and the A1900 target to put the beam at as large of a horizontal angle as allowed by the 4-inch diameter beam pipe without losing a noticeable fraction of the beam. The beam from the K1200 enters the A1900 target by passing roughly from west to east. A positive angle is defined when the beam is north of the optic axis upstream from the target and south of the optic axis downstream (east) from the target. The angle measurement is an approximate value based on where the beam hit viewers along the beamline near the target position. Table 4.2 shows the ^{34}Cl momentum distribution beam settings from the A1900 beam line savesets and how they were handled within the collected experimental data set.

All beam settings of the A1900 fragment separator utilized an Ar^{16+} primary beam at 149.31 MeV/u and a 566.89 mg/cm^2 ^{9}Be production target. Similarly, all settings used a 150 mg/cm^2 Al degrader.

Table 4.2: Four beam setting indicating information obtained from A1900 beam line savesets. B_ρ 1,2,3,4 refers to the magnetic rigidity of the D1, D2, D3 and D4 superconducting dipole magnet. D1 and D2 were set to same B_ρ value and D3 and D4 were set to the same B_ρ value.

Beam setting	Setting title	B_ρ 1,2 (Tm)	B_ρ 3,4(Tm)
1	1st slice up	3.3484	3.2277
2	1st slice down	3.2985	3.1750
3	2nd slice down	3.2819	3.1570
4	3rd slice down	3.2653	3.1389
5	1st slice up -minus 3° at the A1900 target	3.3484	3.2277
6	1st slice up -plus 3° at the A1900 target	3.3484	3.2277

The beam setting difference can be visualized from Fig. 4.10 (a) which shows a plot of the raw events in SeGA vs the time stamp of each event in nanoseconds. Also, projections were taken on the SeGA time axis of Fig. 4.10 (a) to clarify the view on 6 beam settings, which is shown in Fig. 4.10 (b).

The red line on Fig. 4.10 (b) from the left indicates when the beam was turned on for the first beam setting. In this setting, the beam rate gradually reduced. The primary beam is turned off when a sharp drop in activity is observed. Therefore, the red vertical lines brackets the beam-on periods. It might seem that the beam was abruptly turned on and off at the third beam setting, but this is just an indication of drop in beam rate. The time spent in each beam setting is approximately 3.09 hrs, 1.82 hrs, 3.07 hrs, 3.67 hrs, 1.63 hrs, and 2.26 hrs respectively. Also, the binning effects shown in Fig. 4.10(b) did not impact the final results.

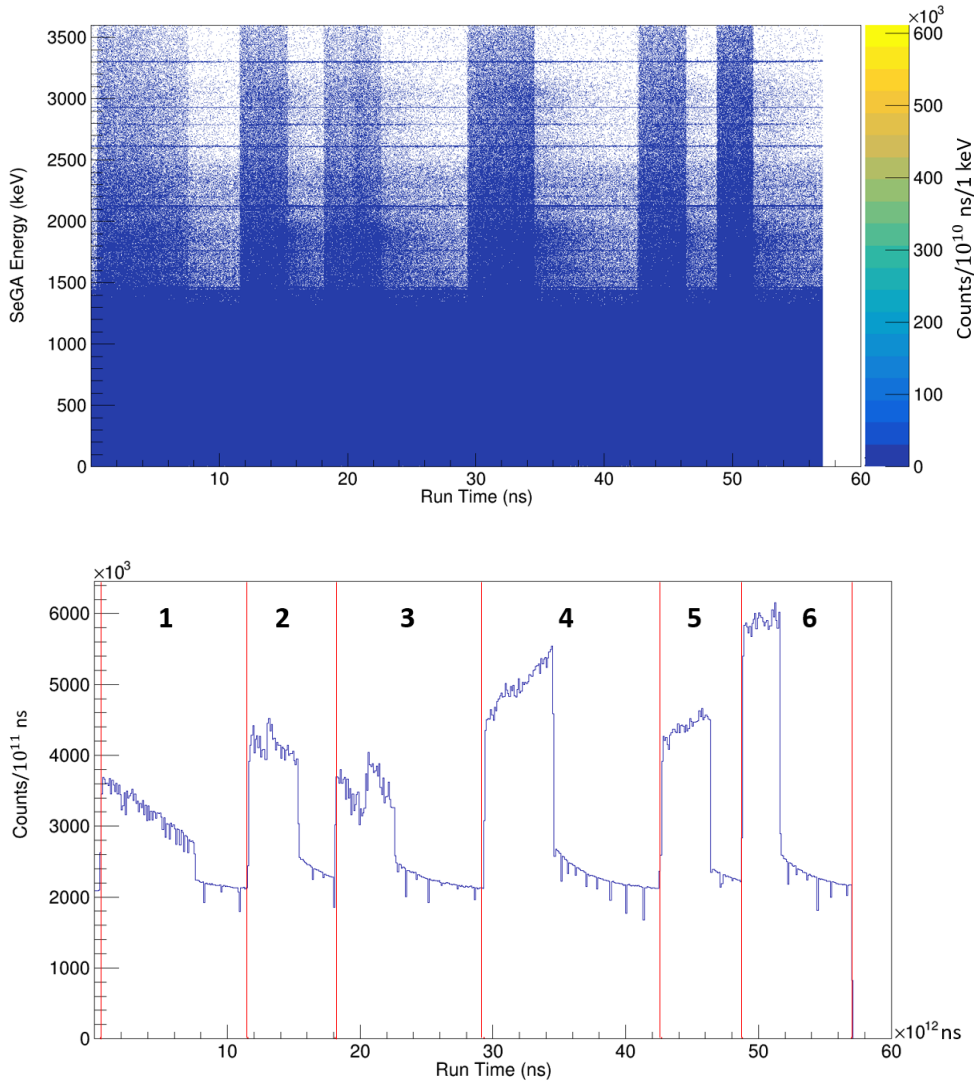

Figure 4.10: (a) (Top)Plot of calibrated energy of raw events in SeGA vs the time stamp of each event in nanoseconds. The 6 vertically dense count area indicates that the experiment utilized 6 beam settings. (b) (Bottom)A spectrum showing counts vs time stamp of each event in SeGA. The red vertical lines are an indication of beam window. For example; the first line from the left is the beam on for the first setting, and the second red line is the beam on for the next beam setting.

In general, the beam time on and off for each settings is shown in Table 4.3.

Table 4.3: Time window for beam settings in nanoseconds.

Beam setting	1	2	3	4	5	6
Beam on (ns) ($\times 10^{13}$)	0.046	1.160	1.830	2.950	4.290	4.890
Beam off (ns) ($\times 10^{13}$)	1.158	1.815	2.934	4.271	4.878	5.703

4.2.3 Time cuts on SeGA spectrum

Following the beam on and beam off time plot (see Fig. 4.10(b)) that indicates the different settings used, we then projected out the γ-ray singles spectra for each of the six settings, thus allowing us to compare the results. This enabled the comparison of the γ peak area corresponding to the three primary lines from ^{34m}Cl decay for each beam setting plots showing each peak presented in Fig. 4.11 - Fig. 4.16.

The strong 1177, 2127 and 3303-keV γ rays are observed as expected. Observation of these gamma rays indicates the presence of ^{34m}Cl in the beam. The areas of these peaks of interest were then fitted in each spectrum, as they are the known peaks associated with ^{34m}Cl (see Fig. 4.2). A γ-ray photopeak has a shape described by a Gaussian distribution given by

$$f(x) = \frac{1}{\sigma\sqrt{2\pi}}\exp(-\frac{1}{2}(\frac{x-\mu}{\sigma})^2) \tag{4.6}$$

where μ is the center of the distribution and σ is the characteristic width. This Gaussian fit was performed on top of a linear background. A single Gaussian fit has five parameters; two to describe the linear background and three to describe the peak (a, μ and σ). The number of counts is determined using

$$A = a\sigma\sqrt{2\pi} \quad \rightarrow \quad \sigma = \frac{FWHM}{2\sqrt{2\ln 2}} \tag{4.7}$$

where a is the height of the peak and σ is the characteristic width which is related to the Full Width at Half Maximum (FWHM).

Table 4.4 shows the γ-ray peak areas for each γ ray for all beam settings along with their associated uncertainties.

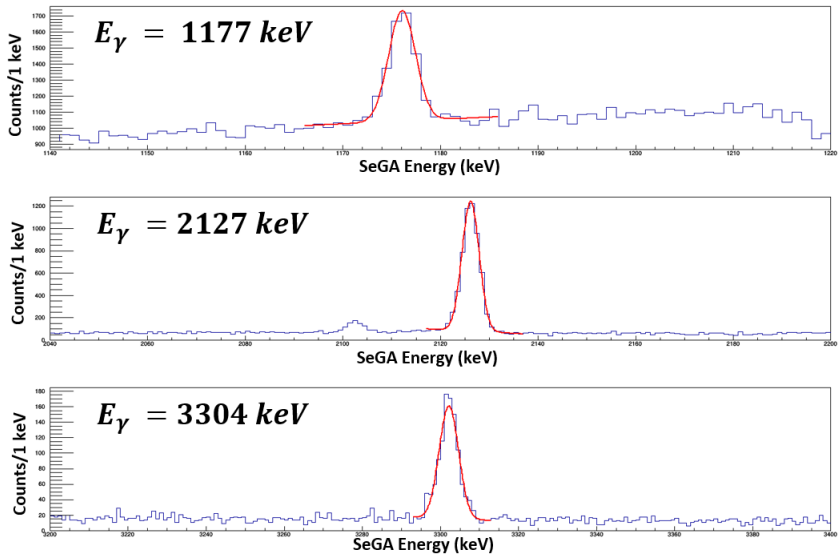

Figure 4.11: Fitted γ peaks (1177 keV, 2127 keV, 3304 keV, respectively) of ^{34m}Cl for Beam Setting 1

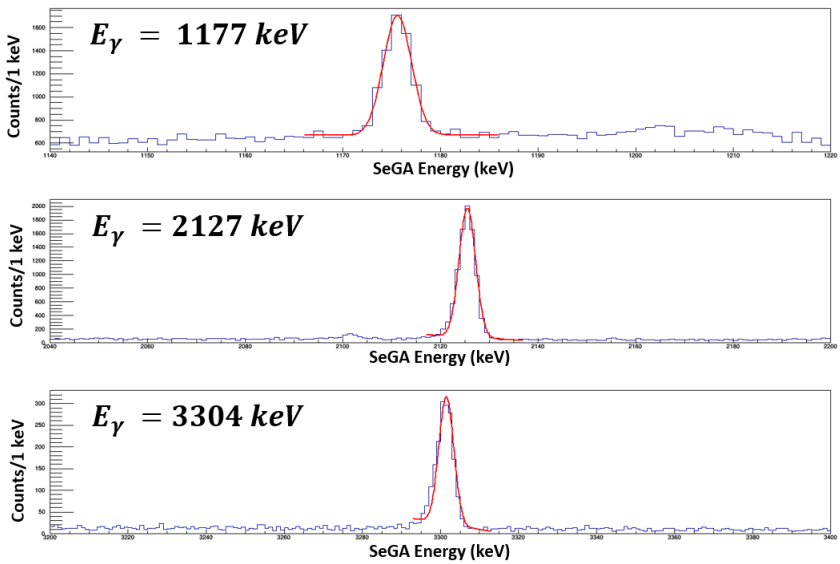

Figure 4.12: Fitted γ peaks (1177 keV, 2127 keV, 3304 keV, respectively) of ^{34m}Cl for Beam Setting 2

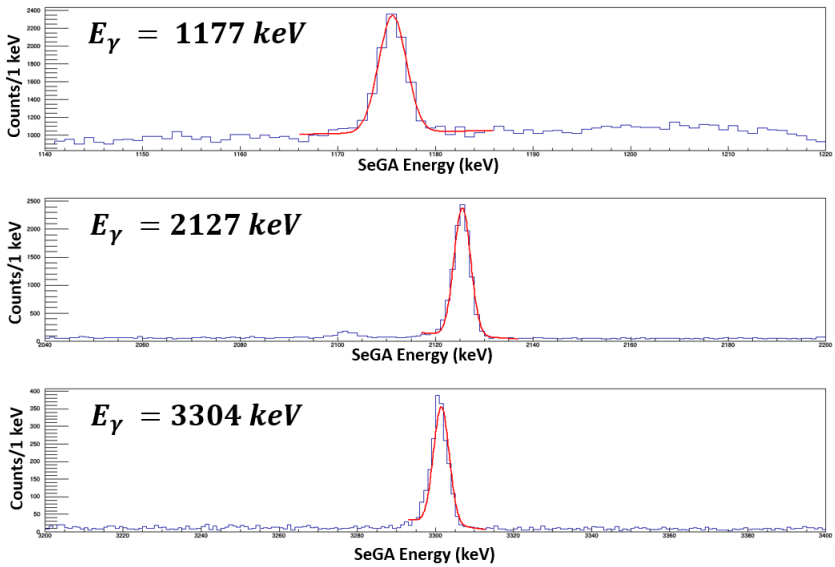

Figure 4.13: Fitted γ peaks (1177 keV, 2127 keV, 3304 keV, respectively) of ^{34m}Cl for Beam Setting 3

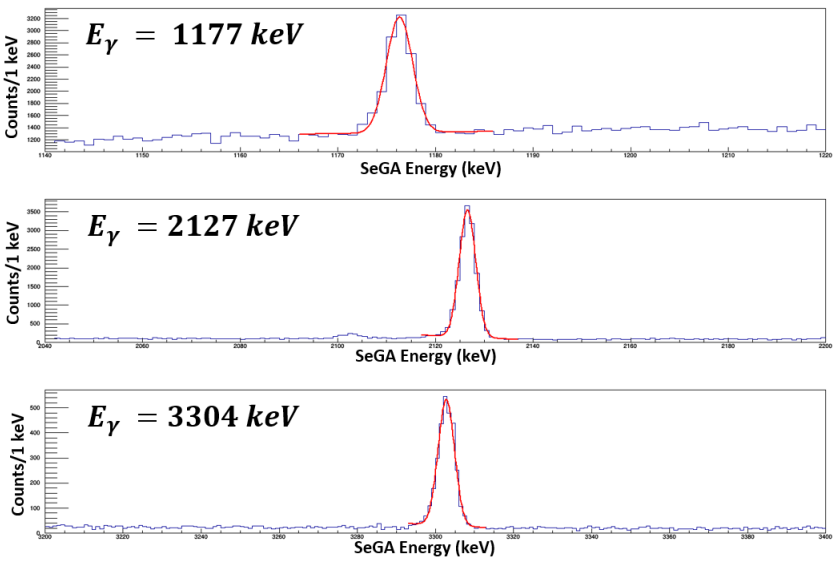

Figure 4.14: Fitted γ peaks (1177 keV, 2127 keV, 3304 keV, respectively) of ^{34m}Cl for Beam Setting 4

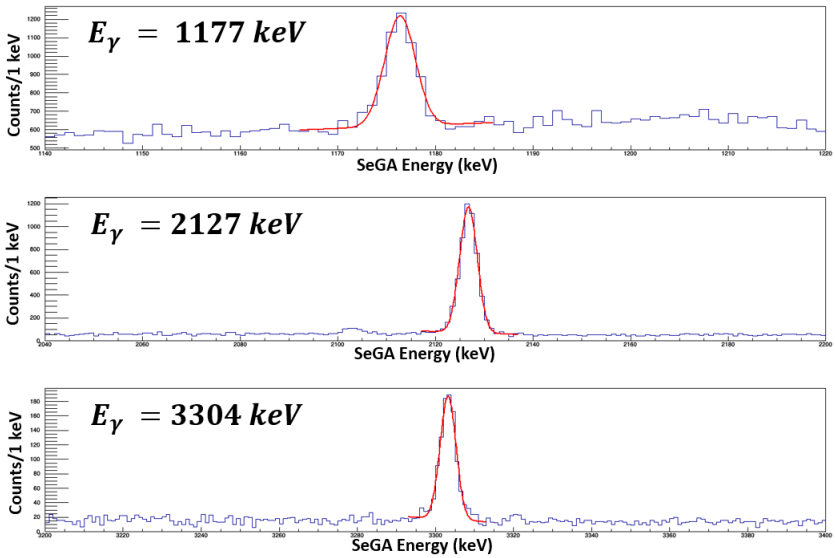

Figure 4.15: Fitted γ peaks (1177 keV, 2127 keV, 3304 keV respectively) of ^{34m}Cl for Beam Setting 5

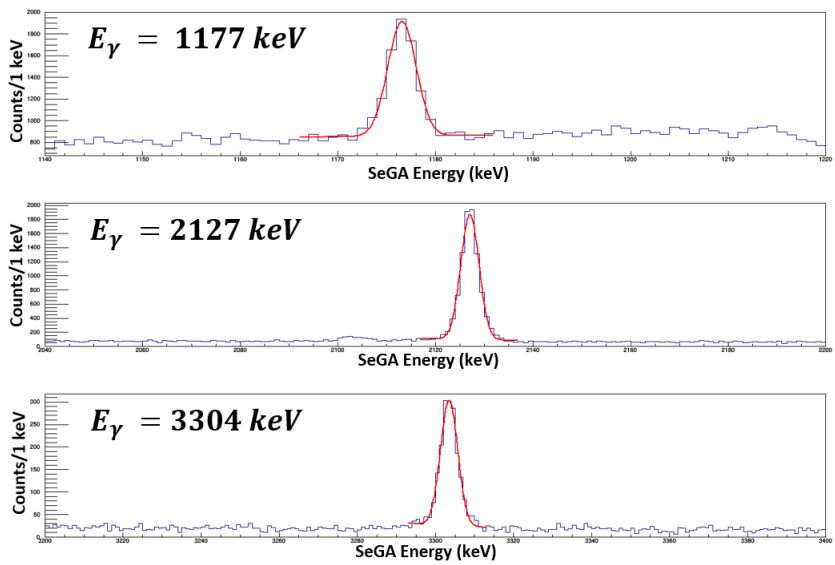

Figure 4.16: Fitted γ peaks (1177 keV, 2127 keV, 3304 keV, respectively) of ^{34m}Cl for Beam Setting 6

Table 4.4: Raw γ-ray peak areas for each ^{34m}Cl γ ray along with γ-ray detector efficiency for all beam settings and their associated uncertainties.

Beam setting	Energy (keV)	Area (Num. of counts)	Efficiency
1	1177	$2.40(17) \times 10^3$	3.23(16)%
	2127	$5.14(12) \times 10^3$	2.28(11)%
	3304	$9.08(63) \times 10^2$	1.64(8)%
2	1177	$3.77(16) \times 10^3$	3.22(16)%
	2127	$8.02(15) \times 10^3$	2.27(11)%
	3304	$14.20(64) \times 10^2$	1.64(8)%
3	1177	$4.72(19) \times 10^3$	3.24(16)%
	2127	$9.73(16) \times 10^3$	2.28(11)%
	3304	$16.80(69) \times 10^2$	1.63(8)%
4	1177	$6.45(22) \times 10^3$	3.22(16)%
	2127	$14.46(20) \times 10^3$	2.30(11)%
	3304	$26.51(89) \times 10^2$	1.64(8)%
5	1177	$2.38(15) \times 10^3$	3.20(16)%
	2127	$4.99(12) \times 10^3$	2.27(11)%
	3304	$8.73(58) \times 10^2$	1.62(8)%
6	1177	$3.87(18) \times 10^3$	3.20(16)%
	2127	$8.30(17) \times 10^3$	2.28(11)%
	3304	$15.46(74) \times 10^2$	1.65(8)%

4.2.4 Branching ratio and efficiency corrections.

Efficiency and branching corrections were used to extract information about the absolute number of ^{34m}Cl ions implanted in the setup. Table 4.4 provides the absolute efficiency photopeak for each γ ray energy of interest for all six beam setting.

The branching ratio for a decay process is the ratio of the number of particles which decay via a specific decay mode with respect to the total number of particles which decay via all decay modes[54]. Branching correction was determined using information from the ENSDF (Evaluated Nuclear Structure Data File)[49]. For example, the 1177 keV γ ray has a relative γ-ray intensity (I_γ) of 32.9, but for absolute intensity per 100 decays, multiply (I_γ) by 0.428. This results in a branching ratio of 14.08%. A similar process was used for 2127-keV and 3303-keV. γ rays collated results for branching ratio are shown in Table 4.5.

Table 4.5: Branching ratios for the ^{34m}Cl γ-ray energies [50].

Energy (keV)	1176	2127	3303
Branching ratio (%)	14.09(24)	42.8(8)	12.29(22)

4.2.5 Absolute numbers of ^{34m}Cl ions implanted

Table 4.6 provides the absolute number of ^{34m}Cl (actual number of ^{34m}Cl), N_{abs}, for each γ-ray energy, E_γ. For determining this absolute number, the following expression was used:

$$N_{\text{abs}}(E_\gamma) = \frac{A}{\text{eff}(E_\gamma) \times BR \times (1 - dt)} \tag{4.8}$$

Table 4.6: Absolute number of ^{34m}Cl determined from each γ ray for all beam settings and their associated uncertainties. These were determined using Eq. 4.8

Beam setting	Energy (keV)	Absolute number of ^{34m}Cl in beam
1	1177	$5.28(47) \times 10^5$
	2127	$5.26(31) \times 10^5$
	3304	$4.51(40) \times 10^5$
2	1177	$8.31(56) \times 10^5$
	2127	$8.24(46) \times 10^5$
	3304	$7.04(49) \times 10^5$
3	1177	$10.32(68) \times 10^5$
	2127	$9.95(55) \times 10^5$
	3304	$8.36(56) \times 10^5$
4	1177	$14.22(89) \times 10^5$
	2127	$14.70(81) \times 10^5$
	3304	$13.13(82) \times 10^5$
5	1177	$5.27(43) \times 10^5$
	2127	$5.13(30) \times 10^5$
	3304	$4.39(37) \times 10^5$
6	1177	$8.60(60) \times 10^5$
	2127	$8.49(48) \times 10^5$
	3304	$7.64(55) \times 10^5$

where A is the observed number of counts in the γ-ray singles spectrum, eff(E_γ) is the absolute photopeak efficiency from Eq. 4.5, BR is the branching ratio given in Table 4.5 and dt is the dead time for data collection. The deadtime is ignored in this analysis (dt~0). To determine N_{abs} for the 1176-keV γ ray with Beam Setting 1, the number of counts in the 1176-keV peak is 2.40(17) $\times 10^3$ from Table 4.4, the absolute photopeak efficiency at 1176 keV is 3.23(16)% from Table 4.4, the branching ratio for the 1176-keV γ ray is 14.09(24)% from Table 4.5 are combined to give

$$N_{\text{abs}}(1177\ keV) = \frac{2.40(17) \times 10^3}{0.0323(16) \times 0.1409(24)} = 5.28(37) \times 10^5 \tag{4.9}$$

Similarly, N_{abs}(2127 keV) for Beam Setting 1 is

$$N_{\text{abs}}(2127\ keV) = \frac{5.14(12) \times 10^3}{0.0228(11) \times 0.428(8)} = 5.26(14) \times 10^5 \tag{4.10}$$

Finally, N_{abs}(3303 keV) for Beam Setting 1 is

$$N_{\text{abs}}(3304\ keV) = \frac{9.08(63) \times 10^2}{0.0164(8) \times 0.1228(22)} = 4.51(31) \times 10^5 \tag{4.11}$$

The same routine is followed for each of the fitted γ rays, with Table 4.6 giving the results. From Table 4.6, we can see that the results for the yield of ^{34m}Cl ions are consistent when utilizing the 1177 keV and 2127 keV γ rays. However, it is also evident that the 3304 keV γ-ray provides a systematically low absolute yield compared to the other γ rays. One possible explanation is an underestimation of its overall intensity produced from the decay of ^{34m}Cl. Despite its systematic lower value, we still averaged it in with the other measured γ-ray results to deduce an overall yield for the ^{34m}Cl within each beam. The weighted average of the ^{34m}Cl absolute yield for each beam settings is then listed in Table 4.7.

Table 4.7: Weighted average number of implanted ^{34m}Cl for each beam setting and their associated uncertainties.

Beam setting	Number of implanted ^{34m}Cl ions
1	$5.04(24) \times 10^5$
2	$7.84(41) \times 10^5$
3	$9.46(60) \times 10^5$
4	$14.01(48) \times 10^5$
5	$4.93(26) \times 10^5$
6	$8.25(31) \times 10^5$

4.3 Identifying implanted ^{34}Cl ions

This section describes how the ^{34}Cl ions were identified using particle identification and the total number of implanted ions was measured. Section 4.3.1 discusses particle identification and ToF information using a Time to Amplitude Converter (TAC) device. Following the discussion of particle identification, the final results for the total number of ^{34}Cl is presented.

4.3.1 Particle identification using ΔE and ToF information

In the experiment 16032A, electrons were completely removed from the ions in the K1200 cyclotron, thereby making the ions fully stripped. This resulted in Q = Z for all charged particles. Therefore the general B_ρ-ΔE-ToF-TKE techniques common to particle identification can be reduced to consider only B_ρ-ΔE-ToF. This technique involves the recorded energy loss (ΔE) of an ion in the PIN detector and the ToF between the image2 scintillator in the A1900 fragment sep-

arator and the first silicon PIN detector. Since the ToF is explicitly proportional to $\frac{A}{Q}$ and ΔE is proportional to Z^2, the identification of each particle can be obtained through a plot of ΔE vs. ToF [32]. This experiment utilized 3 silicon PIN detectors for particle identification, with only one of these primarily used for the analysis and the two others serving as redundant backups in case of a failure.

4.3.2 Determining time of flight

An ion's ToF is determined by the first PIN detector and the image2 scintillator. In the experiment 16032A, the PIN detector is approximately one meter in front of the implantation detector while the image2 scintillator is at the center of the A1900 fragment separator. A Time-to-Amplitude-Converter (TAC) is used to record the time of flight signal. A TAC is a device that receives input signals on its start and stop terminals, and generates an amplitude pulse based on the time delay between the two input signals. Based on this limitation that the TAC is dead for a relatively long amout of time if it receives a start with no stop, the start signal comes from the PIN detector and the stop signal comes from the image2 scintillator. To output a positive TAC time difference, a signal delay is placed on the image2 scintillator.

4.3.3 Determining the number of ^{34}Cl for each beam setting

In order to determine the isomer ratio of ^{34m}Cl to ^{34}Cl for each beam setting, the number of implanted ^{34}Cl ion had to be determined using particle identification. If the half-life is short compared to the overall implantation rate, the particle identification can be determined by correlating each implanted ion into the $CeBr_3$ detector to its decay, then looking at its subsequent decay. An implant is detected by both the $CeBr_3$ implantation detector and the first PIN detector while a decay

is detected by only the $CeBr_3$ implantation detector. However, the number of ^{34}Cl ions could not be determined by plotting its β-delayed γ spectrum because ^{34}Cl has a very long half-life of 31.99(3) minutes compared to the overall implantation rate.

In place of using the implantation and PIN detector to determine the implanted ^{34}Cl ions, the A1900 PID plot was referenced for particle identification. The counting of the passage of heavy ions through the A1900 fragment separator is based on an event-by-event basis by utilizing the cyclotron RF and a 528 μm Si PIN diode detector for ToF and $\triangle$E determinations.

As discussed in Sec. 3.5, the experiment 16032A utilized a 49mm $\times$ 49mm $\times$ 3mm thick $CeBr_3$ implantation detector coupled with a PSPMT for detection of β-decay electrons. The implantation depth distributions for each beam setting using LISE++ are presented in Fig. 4.3 - Fig. 4.8.

Utilizing the techniques developed in Section 4.3.1, the PID plot for six beam settings showing ions implanted into the $CeBr_3$ implantation detector are displayed in Fig. 4.17 - Fig. 4.22. The plots were generated by using the ions energy loss in the first PIN detector and information on ToF between the image2 scintillator and the first PIN detector.

The PID plot for Beam Setting 1 (Fig. 4.17) indicates that ^{32}P, ^{33}S and ^{34}Cl ions were implanted into the $CeBr_3$ implantation detector. As discussed earlier, ^{34}Cl could not be determined using a β-delayed γ spectrum because it has a long half life of 31.99(3) minutes compared to the overall implantation rate.

The half-life of ^{32}P ($T_{1/2}$ = 14.268(5) days) is too long for correlation of an implanted ^{32}P ion to its decay to occur. Also, there is no β-delayed γ-ray spectrum for ^{33}S because it is a stable isotope that does not decay.

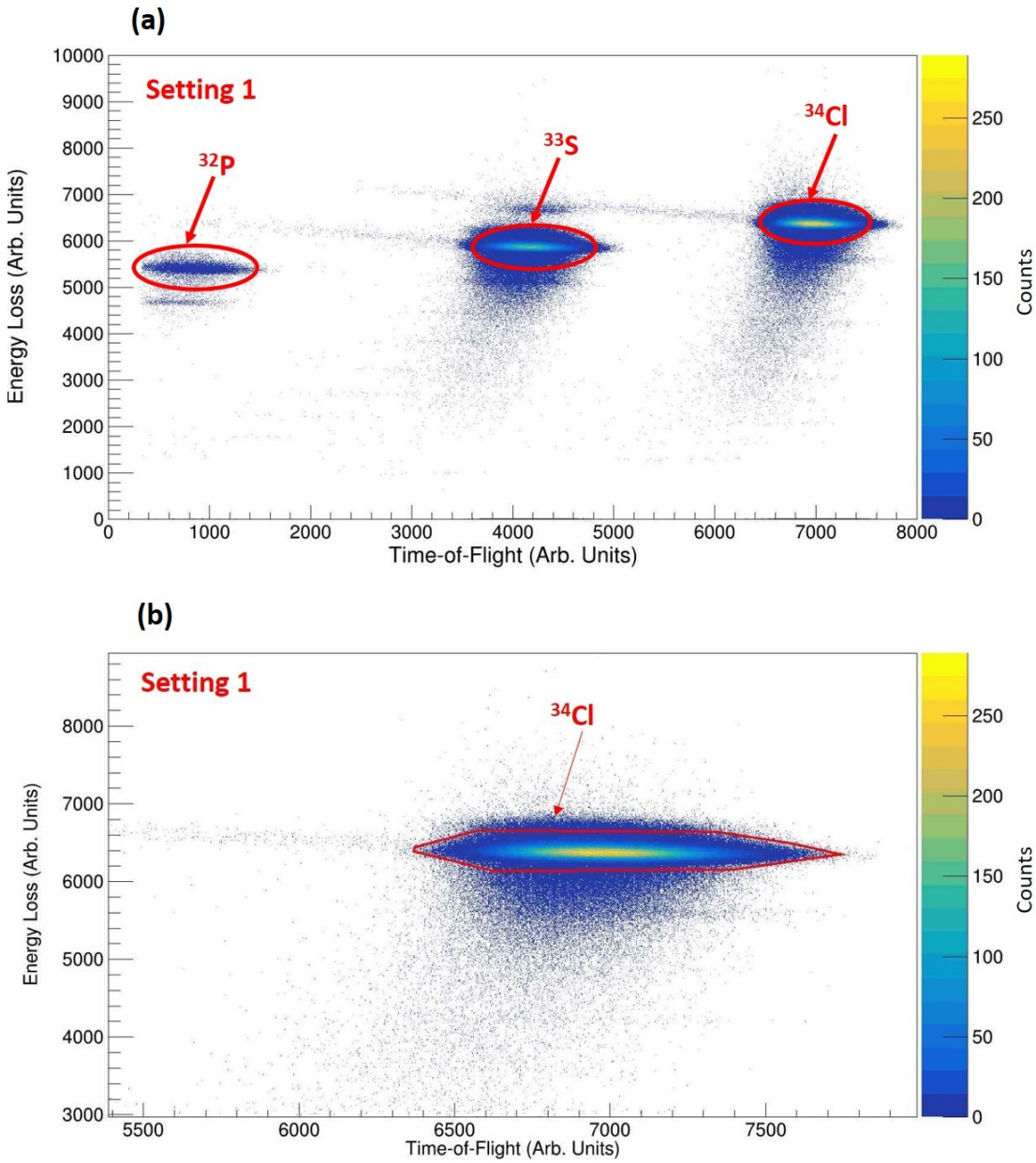

Figure 4.17: (a)Particle identification plot for Beam Setting 1 showing ions implanted into the $CeBr_3$ implantation detector. On the x-axis is the time of flight while on the y-axis is the energy loss. (b) Graphical cut used to determine the total number of ^{34}Cl for this setting.

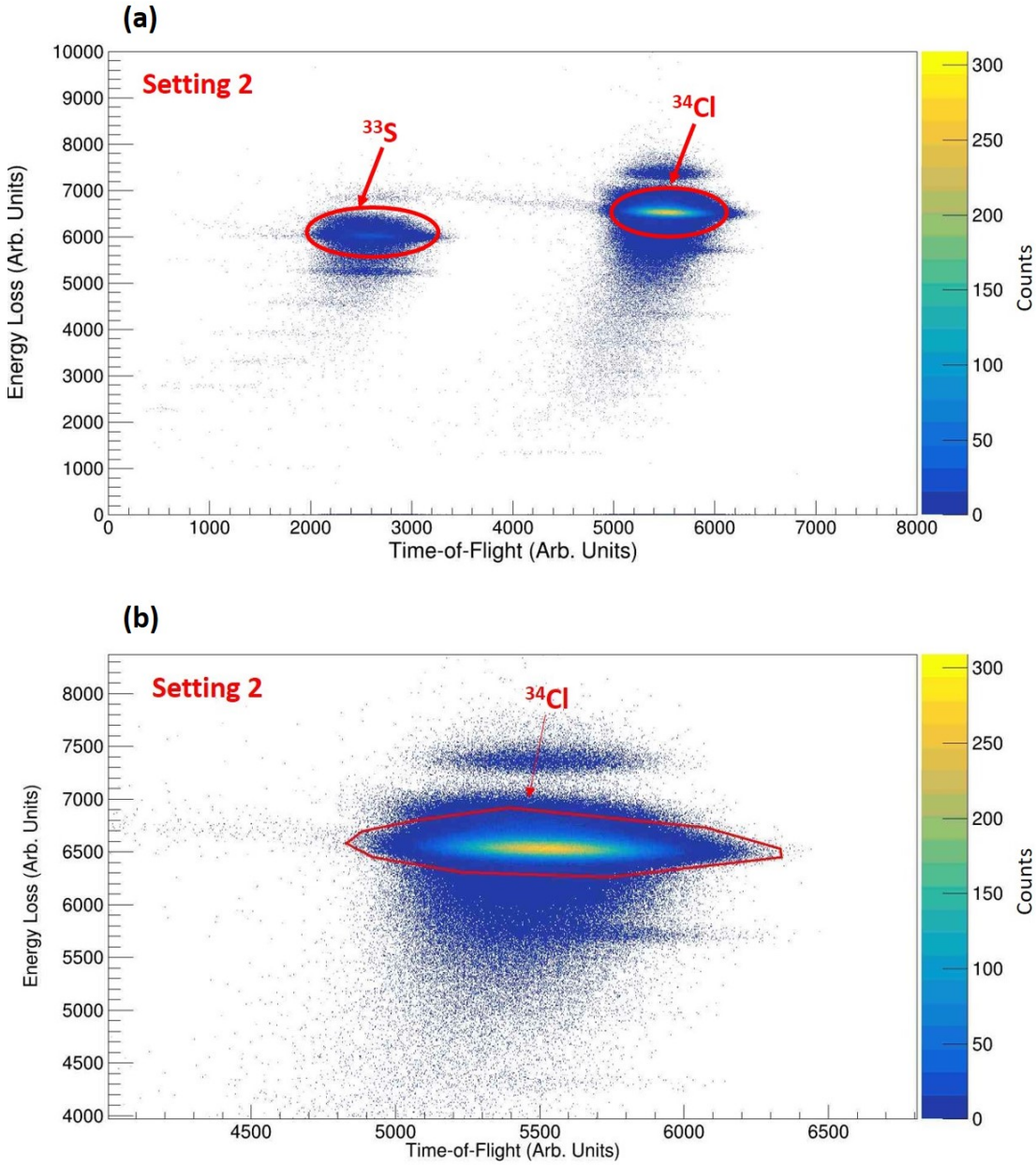

Figure 4.18: (a)Particle identification plot for Beam Setting 2 showing ions implanted into the $CeBr_3$ implantation detector. On the x-axis is the time of flight while on the y-axis is the energy loss. (b) Graphical cut used to determine the total number of ^{34}Cl for this setting.

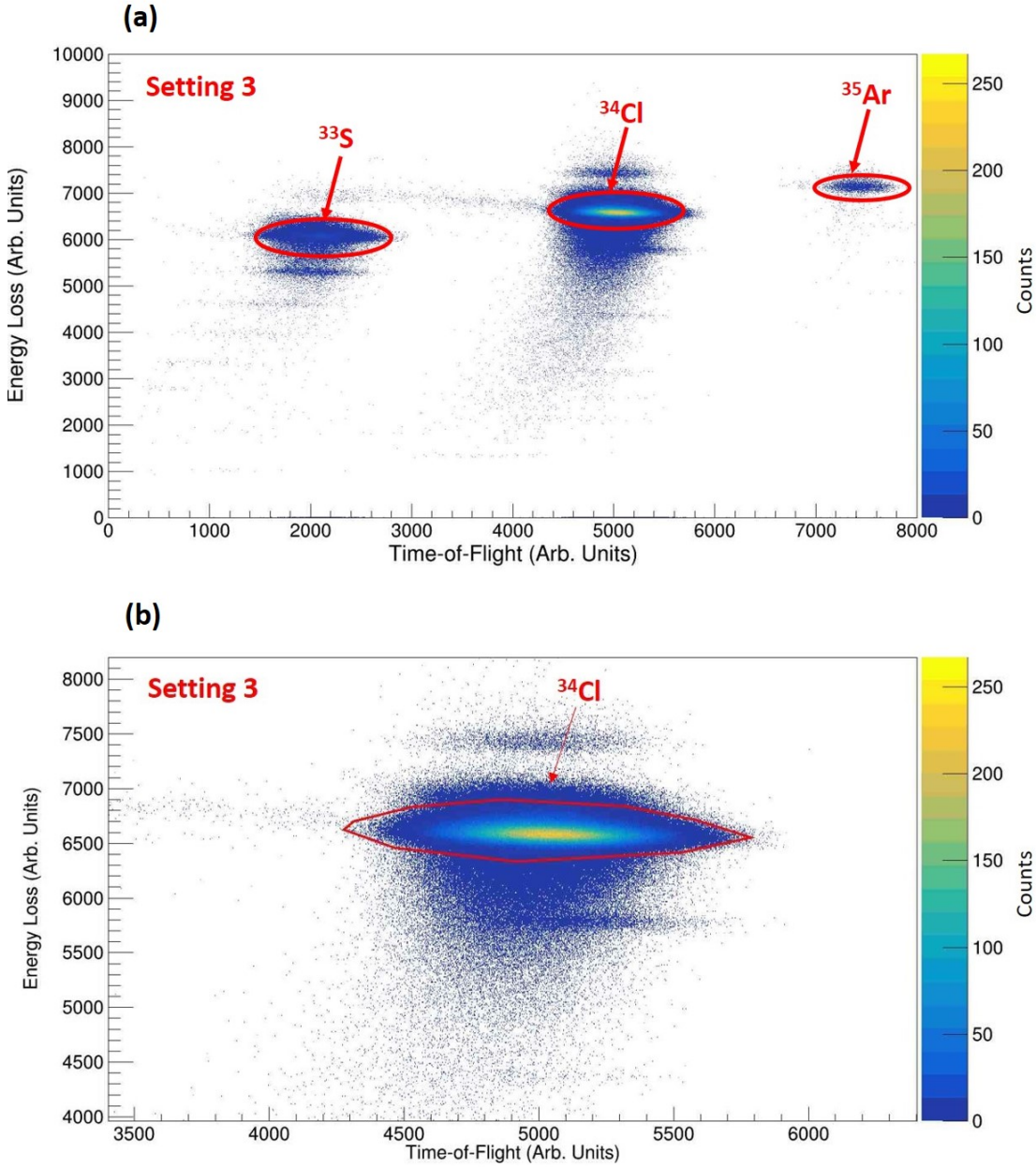

Figure 4.19: (a)Particle identification plot for Beam Setting 3 showing ions implanted into the $CeBr_3$ implantation detector. On the x-axis is the time of flight while on the y-axis is the energy loss. (b) Graphical cut used to determine the total number of ^{34}Cl for this setting.

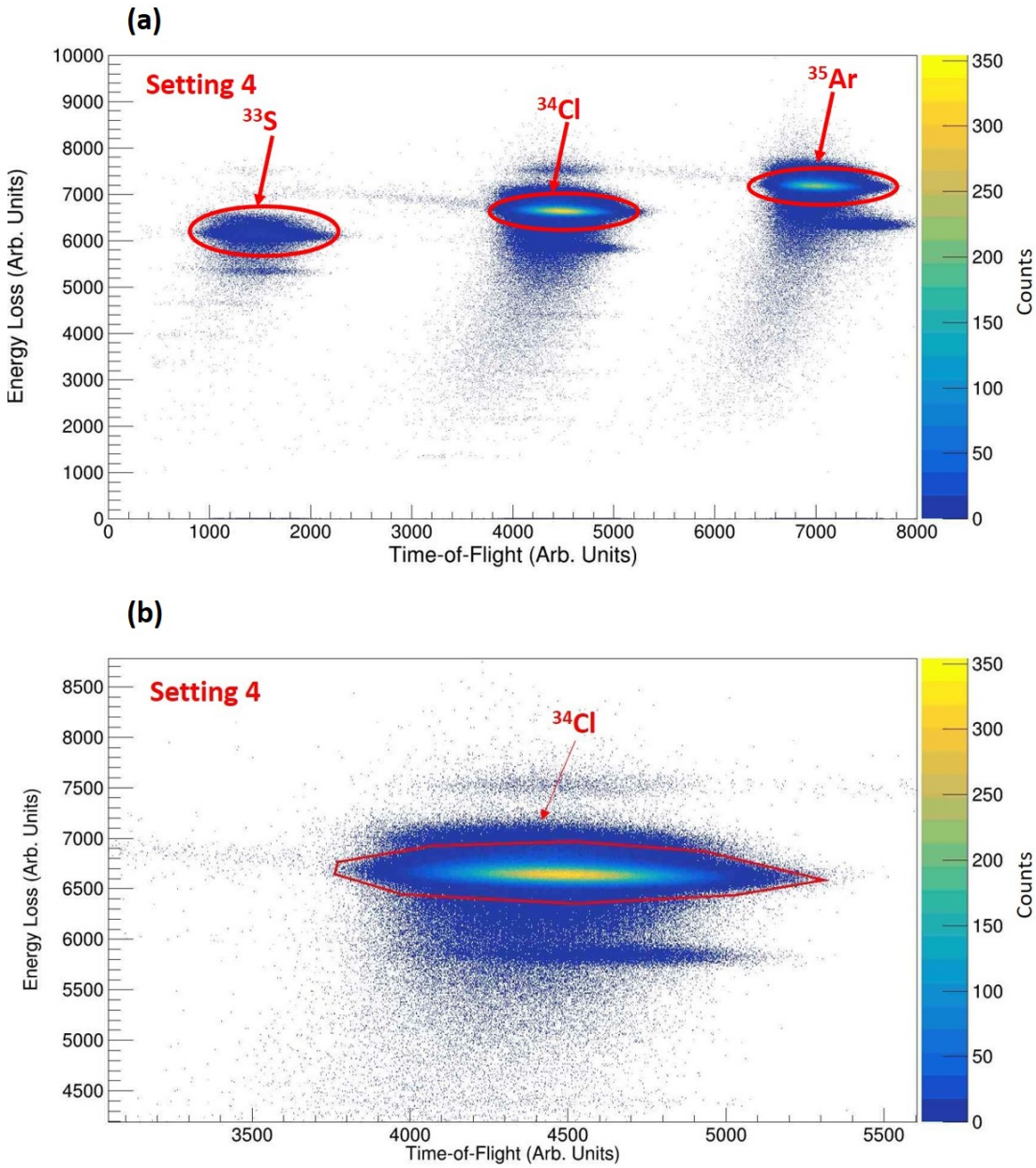

Figure 4.20: (a)Particle identification plot for Beam Setting 4 showing ions implanted into the $CeBr_3$ implantation detector. On the x-axis is the time of flight while on the y-axis is the energy loss. (b) Graphical cut used to determine the total number of ^{34}Cl for this setting.

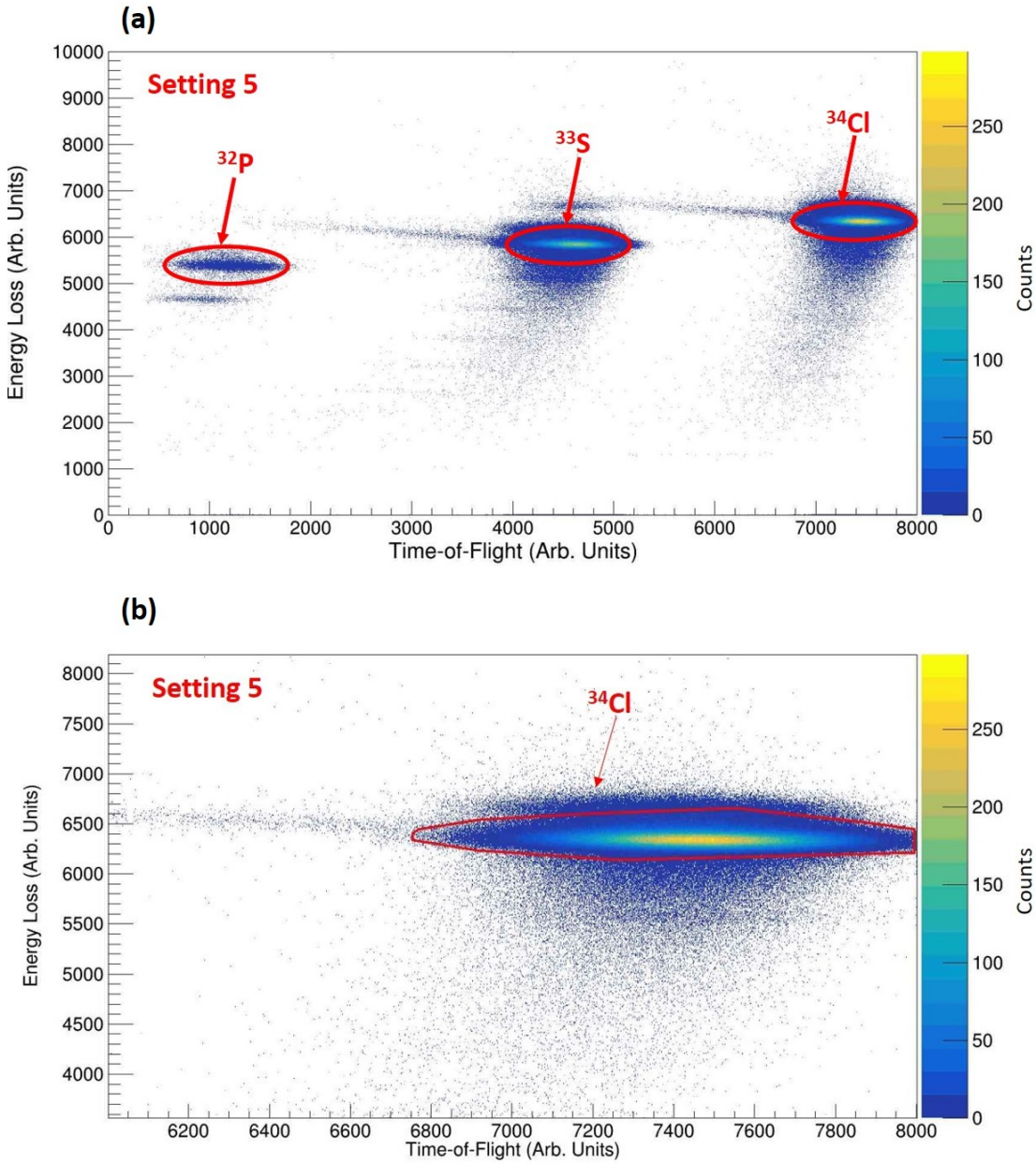

Figure 4.21: (a)Particle identification plot for Beam Setting 5 showing ions implanted into the $CeBr_3$ implantation detector. On the x-axis is the time of flight while on the y-axis is the energy loss. (b) Graphical cut used to determine the total number of ^{34}Cl for this setting.

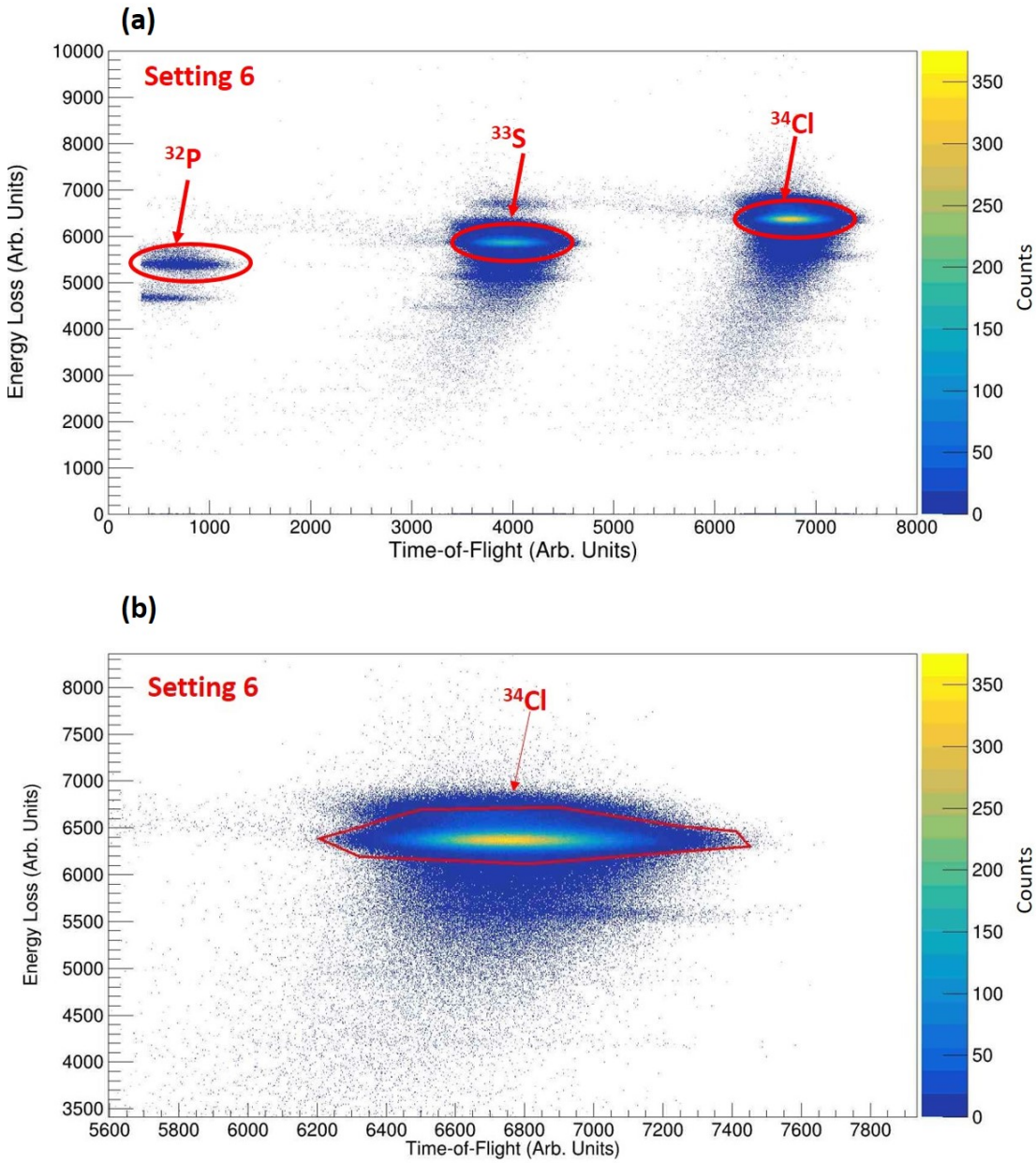

Figure 4.22: (a)Particle identification plot for Beam Setting 6 showing ions implanted into the $CeBr_3$ implantation detector. On the x-axis is the time of flight while on the y-axis is the energy loss. (b) Graphical cut used to determine the total number of ^{34}Cl for this setting.

Beam Setting 2 and 3 PID plots (Fig. 4.18 and Fig. 4.19 respectively) display ^{33}S and ^{34}Cl ion implantation. Beam Setting 3 plot additionally shows ^{35}Ar was implanted into the $CeBr_3$ implantation detector. The ^{35}Ar could not be determined from a β-delayed γ-ray spectrum because 98.23% of the time it decays from its ground state, $J^\pi = 0^+$, to the ground state of ^{35}Cl, without emission of a γ ray. Effort was made to find ^{35}Ar in the correlated γ-ray spectra since it has an half-life of 1.7756(10) s, but the next highest order from intensity in ^{35}Ar was too small (I_{abs} = 0.249%) to be observed in the β-delayed γ-ray spectrum. Beam Setting 4 indicates ^{33}S, ^{34}Cl and ^{35}Ar. Lastly, Beam Setting 5 and 6 all show ^{32}P, ^{33}S and ^{34}Cl was implanted into the detector.

4.3.4 Graphical cuts on the PID spectrum

To determine the total number of ^{34}Cl ions implanted in the setup, a conservative approach was taken by applying a large graphical cut as shown in Fig. 4.17 - Fig. 4.22. These large graphical cuts was used as a compromise to maximize the number of ^{34}Cl ions that were included in the final result. The number of implanted ^{34}Cl ion was then determined by taking the integrals of the large graphical cuts. The uncertainties was estimated from the square root of the integral of the graphical cut. There is an ongoing analysis to quantify the consistency of the graphical cuts used in Fig. 4.17 - Fig. 4.22.

In conclusion, the number of ^{34}Cl ions implanted into the $CeBr_3$ detector during experiment 16032A for each beam setting is shown in Table 4.8.

4.3.4.1 Determining transmission efficiency to the $CeBr_3$ implantation detector.

The PID plots shown in Fig. 4.17 - Fig. 4.22 display ions which were detected by either the first PIN detector or both the $CeBr_3$ and the first PIN detector. This means that not all ions that

Table 4.8: Number of ^{34}Cl isotope implanted into $CeBr_3$ for each beam setting.

Beam Setting	Number of Implanted ^{34}Cl ions
1	$1.7709(13) \times 10^6$
2	$2.2355(15) \times 10^6$
3	$1.7449(13) \times 10^6$
4	$2.6679(16) \times 10^6$
5	$1.7377(13) \times 10^6$
6	$2.3482(15) \times 10^6$

were detected by the PIN detector will finally be implanted into the $CeBr_3$. Only ions that implant in our $CeBr_3$ implantation detector could have γ rays emitted from their decay observed in the SeGA spectra. The transmission efficiency is then required to determine the overall probability that ions passing through the PIN detectors subsequently implant into the $CeBr_3$ implantation detector. Transmission efficiency of the $CeBr_3$ is the probability that ions detected in the PIN detector are also implanted into the $CeBr_3$ detector.

To determine the transmission efficiency for Beam Setting 1, the total counts of the PSPMT dynode energy (indicating a signal in the $CeBr_3$ implantation detector) was determined in coincidence with a signal in the PIN detector and a PIN energy condition that excludes the possibility of light ions that are unlikely to implant (see Fig. 4.23(a) and Table 4.9). Then, the number of counts in the first PIN energy spectrum with the same energy condition so as to exclude the possibility of light ions was also determined (see Fig. 4.23(b) and Table 4.9). Therefore, the transmission efficiency to the $CeBr_3$ implantation detector was determined by dividing the total counts of the

PSPMT dynode energy by the integrated PIN energy spectrum counts. Table 4.9 shows the transmission efficiency of each beam setting. As expected, the transmission is very high ($\sim$ 100%) because the PIN detector is located very close to the $CeBr_3$ implantation detector (approximately 1 meter upstream).

Table 4.9: Transmission efficiency from the first PIN detector to the $CeBr_3$ implantation detector for each beam setting.

Beam Setting	$CeBr_3$ counts	PIN counts	Transmission efficiency (%)
1	3.1490×10^6	3.1540×10^6	99.84
2	2.6790×10^6	2.6840×10^6	99.81
3	2.0400×10^6	2.0440×10^6	99.80
4	4.9160×10^6	4.9250×10^6	99.82
5	3.3210×10^6	3.3280×10^6	99.79
6	4.0380×10^6	4.0460×10^6	99.80

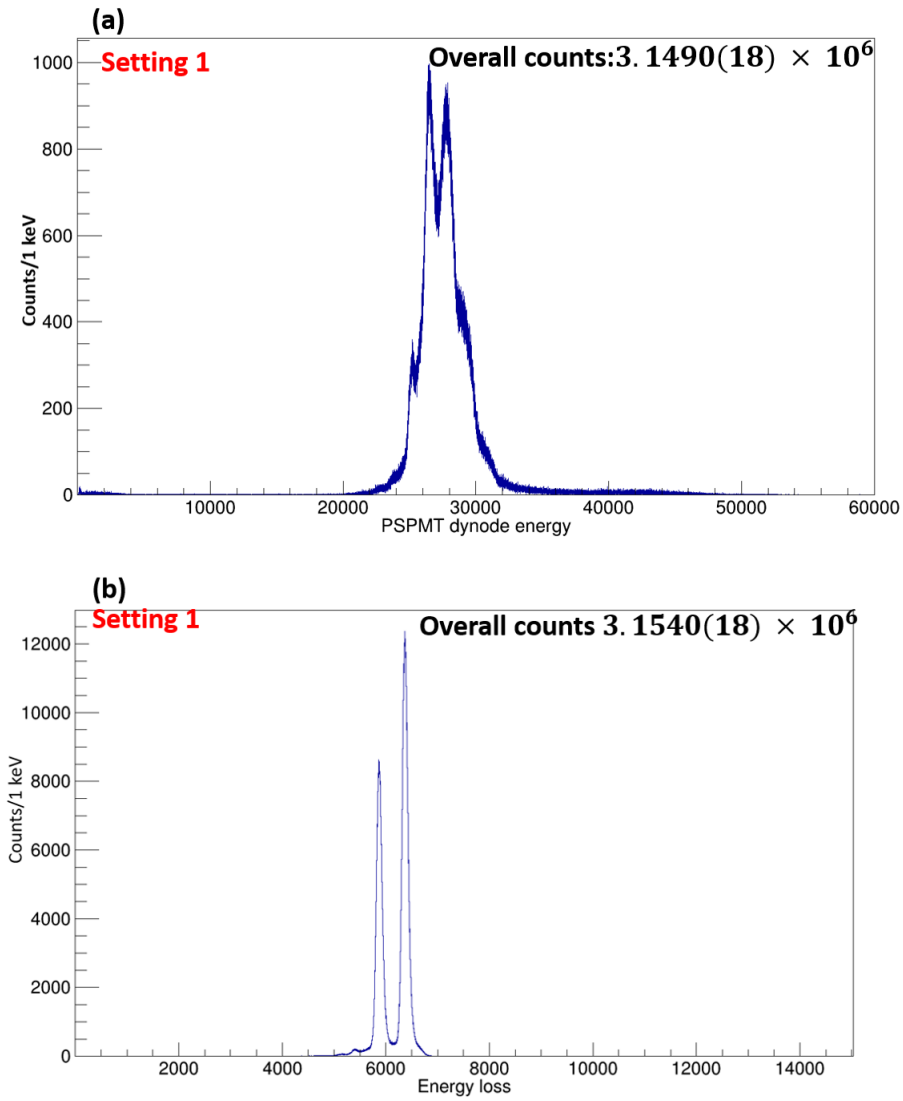

Figure 4.23: (a)$CeBr_3$ implantation spectrum showing the PSPMT dynode energy. (b) PIN spectrum showing the energy loss in the PIN detector. The transmission efficiency to the implantation detector will be the ratio of number at the top right corner in (a) to the number at the top right corner in (b).

4.4 Isomeric ratio of ^{34}Cl

From Table 4.7, Table 4.8 and Table 4.9, the isomeric state content ratio of ^{34}Cl for Beam Setting 1 is calculated as follow:

$$\begin{aligned}&\frac{\text{Number of ions of } ^{34m}\text{Cl implanted}}{\text{Number of overall ions in the } ^{34}\text{Cl beam}} \div \text{Transmission efficiency} \\ &= \frac{5.04(24) \times 10^5}{1.7709(13) \times 10^6} \div 0.9984 = 28.5(14)\%\end{aligned} \tag{4.12}$$

By following similar pattern, Table 4.10 represents the final result for the isomeric state content ratio of each Beam Setting for ^{34}Cl. Since the number of ^{34m}Cl is divided by the number of implanted ^{34}Cl ions, any fluctuations in beam intensity from the cyclotrons are normalized between the different beam settings.

Table 4.10: Isomeric state content ratio of each beam setting in ^{34}Cl.

Beam setting	Isomeric content ratio of ^{34}Cl beam
1	28.5(14)%
2	35.2(19)%
3	54.3(34)%
4	52.6(18)%
5	28.4(15)%
6	35.2(13)%

CHAPTER V

CONCLUSION

One of the main motivation for this experiment was to determine the Beam Setting to maximize production of ^{34m}Cl. By maximizing the production of ^{34m}Cl, the highest abundant isomeric ratio will be used to study the single neutron occupancies in high Mirror Energy Difference for ^{35}Cl. The importance of this measurement helps with the testing of single-particle aspects of the MED states by extracting single neutron overlaps. Sec. 1.5 gives a detailed description for the motivation of this experiment.

From the final result of the isomeric ratio of ^{34}Cl for the six Beam Settings shown in Table 4.10, Beam Setting 3 and Beam Setting 4 produces the highest isomer ratio of 54.3(34)% and 52.6(18)% respectively. These settings has been recommended for use at the NSCL to study the single neutron occupancy in ^{35}Cl.

The result presented in this work does not include an analysis using the Batemann equation. The time binning of the spectra for Bateman equation analysis has been developed. Ongoing analysis is being done to fit the Bateman equation, which requires proper determination of both the production and decay rates. Low statistics has made the analysis challenging thus far and we currently lack full beam intensity information to perform the analysis accurately. We hope to have the information soon.

Another future project focuses on building a better consistency for normalizing the graphical cuts used to determine the final purities (Fig. 4.17 - Fig. 4.22). While conservative cuts were utilized within uncertainty between one another, the differences in overall ToF between each A1900 setting means a more exact normalization should be utilized. We will be working with the A1900 group at the NSCL to finalize this aspect of the analysis.

REFERENCES

[1] J. I. Prisciandaro, *Beta Decay Studies of ^{69}Ni and ^{58}V: Development of subshell gaps within the N= 28-50 shell*. PhD thesis, PhD thesis, Michigan State University, 2001. https://publications.nscl.msu.edu/thesis/Prisciandaro_2001_131.pdf.

[2] E. Rutherford, "LXXIX. The scattering of α and β particles by matter and the structure of the atom," *The London, Edinburgh, and Dublin Philosophical Magazine and Journal of Science*, vol. 21, no. 125, pp. 669–688, 1911. http://mrmackenzie.co.uk/podpress_trac/feed/3110/0/Rutherford-paper.pdf.

[3] H. Gegier and E. Marsden, "On a diffuse reflection of the α-particles," *Proceedings of the Royal Society of London. Series A, Containing Papers of a Mathematical and Physical Character*, vol. 82, no. 557, pp. 495–500, 1909. http://web.ihep.su/dbserv/compas/src/geiger09/eng.pdf.

[4] A. S. Panchbhai *et al.*, "Wilhelm Conrad Röntgen and the discovery of X-rays: Revisited after centennial," *Journal of Indian academy of oral medicine and radiology*, vol. 27, no. 1, p. 90, 2015. http://www.jiaomr.in/article.asp?issn=0972-1363;year=2015;volume=27;issue=1;spage=90;epage=95;aulast=Panchbhai.

[5] P. Gasparini, "History of radioactivity," in *Uranium geochemistry, mineralogy, geology, exploration and resources*, pp. 1–3, Springer, 1984. https://link.springer.com/chapter/10.1007/978-94-009-6060-2_1.

[6] N. Fröman, "Marie and Pierre Curie and the discovery of polonium and radium," *Palestra na royal swedish academy of sciences, em Estocolmo, Suécia*, 1996. https://www.nobelprize.org/prizes/uncategorized/marie-and-pierre-curie-and-the-discovery-of-polonium-and-radium-2/?print=1&guid=on.

[7] R. H. Paul Peter Urone, *College physics*. Opentextbc, 2012. https://opentextbc.ca/universityphysicsv3openstax/chapter/nuclear-binding-energy.

[8] H. L. Crawford, *Evolution of nuclear shell structure: β-decay and isomeric properties of nuclei in and near the fp shell*. Michigan State University, 2010. https://groups.nscl.msu.edu/nscl_library/Thesis/Crawford,%20Heather.pdf.

[9] S. R. Stroberg, *Single-particle structure of neutron-rich silicon isotopes and the breakdown of the N= 28 shell closure*. Michigan State University, 2014. https://pdfs.semanticscholar.org/2d5f/8567374a73b8842cbd809180cacbf6e41bf3.pdf.

[10] O. Haxel, J. H. D. Jensen, and H. E. Suess, "On the "magic numbers"in nuclear structure," *Physical Review*, vol. 75, no. 11, p. 1766, 1949. https://link.aps.org/pdf/10.1103/PhysRev.75.1766.2.

[11] M. G. Mayer, "On closed shells in nuclei. II," *Physical Review*, vol. 75, no. 12, p. 1969, 1949. https://link.aps.org/pdf/10.1103/PhysRev.75.1969.

[12] A. Bohr and B. Mottelson, "Nuclear Structure. vol. 2. Nuclear Deformations," 1975.

[13] G. K.K, *Studies of shape changes of deformed nuclei and its effects on cluster emission*. Department of physics, University of Calicut, 2012. https://shodhganga.inflibnet.ac.in/handle/10603/88449.

[14] M. R. Mumpower, T. Kawano, J. L. Ullmann, M. Krtička, and T. M. Sprouse, "Estimation of M 1 scissors mode strength for deformed nuclei in the medium-to heavy-mass region by statistical Hauser-Feshbach model calculations," *Physical Review C*, vol. 96, no. 2, p. 024612, 2017. https://journals.aps.org/prc/abstract/10.1103/PhysRevC.96.024612.

[15] L. Bildsten, "Thermonuclear burning on rapidly accreting neutron stars," in *NATO Advanced Science Institutes (ASI) Series C*, vol. 515, p. 419, 1998. https://ui.adsabs.harvard.edu/abs/1998ASIC..515..419B/abstract.

[16] C. Iliadis, A. Champagne, J. José, S. Starrfield, and P. Tupper, "The effects of thermonuclear reaction-rate variations on nova nucleosynthesis: A sensitivity study," *The astrophysical Journal supplement series*, vol. 142, no. 1, p. 105, 2002. https://iopscience.iop.org/article/10.1086/341400/meta.

[17] P. Banerjee, G. W. Misch, S. K. Ghorui, and Y. Sun, "Effective stellar β-decay rates of nuclei with long-lived isomers: Al 26 and Cl 34," *Physical Review C*, vol. 97, no. 6, p. 065807, 2018. https://journals.aps.org/prc/abstract/10.1103/PhysRevC.97.065807.

[18] OpenStax, *College Physics*. Open Stax, 2012.

[19] G. T. S. Walter Loveland, David J. Morissey, *Modern nuclear chemistry*. John Wiley and Sons, Inc., Hoboken, New Jersey, 2006. https://www.academia.edu/32900226/Modern_Nuclear_Chemistry_2nd_ed_-_Walter_D._Loveland_et_al._Wiley_2017_.

[20] G. Gilmore, *Practical gamma-ray spectroscopy*. John Wiley & Sons, 2011. https://www.tandfonline.com/doi/pdf/10.3109/00016925909173730.

[21] L. G. S. D. G. Sarantites, *Introduction to the atomic nucleus*. Washington, St Louis, 2012. http://chemistry.wustl.edu/ dgs/chem436/Lectures/Chem-436-Lecture_notes.pdf.

[22] hyperphysics, *hyperphysic*. Scilinks, 2001. http://hyperphysics.phy-astr.gsu.edu/hbase/quantum/fermi2.html#c1.

[23] W. Meyerhof, *Elements of nuclear physics*. McGraw-Hill, New York, 1967. https://ocw.mit.edu/courses/nuclear-engineering/22-101-applied-nuclear-physics-fall-2006/lecture-notes/lec22.pdf.

[24] D. J. Morrissey, G. T. Seaborg, and W. D. Loveland, *Modern Nuclear Chemistry.* John Wiley & Sons, 2006.

[25] L. van Dommelen, *Quantum mechanics for engineers*. Dommelen, 2004. http://www.eng.fsu.edu/ dommelen/quantum/style_a/index.html.

[26] G. Friedlander, J. W. Kennedy, E. S. Macias, and J. M. Miller, *Nuclear and radiochemistry*. John Wiley & Sons, 1981.

[27] K. S. Krane, D. Halliday, *et al.*, *Introductory nuclear physics*. John Wiley & Sons, Inc., New York, 1987.

[28] G. Nelson and D. Reilly, "Gamma-ray interactions with matter," *Passive nondestructive analysis of nuclear materials*, pp. 27–42, 1991. http://www.sciencemadness.org/lanl1_a/lib-www/la-pubs/00326397.pdf.

[29] S. N. Liddick, *Beta-decay Studies of Neutron-rich Nuclides and the Possibility of an N: 34 Subshell Closure*. PhD thesis, Michigan State University. Department of Chemistry, 2004. http://publications.nscl.msu.edu/thesis/Liddick_2004_195.pdf.

[30] J. Cetnar, "General solution of Bateman equations for nuclear transmutations," *Annals of Nuclear Energy*, vol. 33, no. 7, pp. 640–645, 2006. https://www.sciencedirect.com/science/article/pii/S0306454906000284?casa_token=F_7tcitHUZkAAAAA:KouI8XR0e76YKqcUYnYA6XM7zNRXIn6L96bmsxcNqstx6vXbz0qFNqxmRgUaN8WAAuxzGReyt_lu.

[31] A. Gade and B. Sherrill, "NSCL and FRIB at Michigan State University: Nuclear science at the limits of stability," *Physica Scripta*, vol. 91, no. 5, p. 053003, 2016. https://iopscience.iop.org/article/10.1088/0031-8949/91/5/053003/pdf.

[32] C. J. Prokop, *Shape coexistence in the neutron-rich nickel isotopes near N= 40*. Michigan State University, 2016. https://pdfs.semanticscholar.org/a66f/4c1bd570c96af242332694eec3f79842e477.pdf.

[33] D. Morrissey, "The coupled cyclotron project at the NSCL," *Nuclear Physics A*, vol. 616, no. 1-2, pp. 45–55, 1997. https://www.sciencedirect.com/science/article/pii/S0375947497000730.

[34] C. T. Ramsell, *Experimental study of an ion cyclotron resonance accelerator*. PhD thesis, Michigan State University. Department of Physics and Astronomy, 2000. https://ieeexplore.ieee.org/stamp/stamp.jsp?arnumber=792423.

[35] J. Bin, Z. Zhen-Lu, Z. Tian-Jue, X. Jian-Sheng, W. Xiu-Long, Y. Zhi-Guo, H. Shi-Gang, and X. Le, "Theoretical and Practical study on RF Model Cavity of 100mev H-Cyclotron," *Chinese Physics C*, vol. 32, no. S1, pp. 160–162, 2008. http://cpc.ihep.ac.cn/article/id/97e18b16-cd0d-42f0-be93-c4c9e9ac5a94.

[36] P. K. Sigg, "RF for cyclotrons," 2006. https://cds.cern.ch/record/1005053/files/p231.pdf.

[37] S. M. Lund, "Accelerator physics." Exotic beam summer school, Michigan State university, National Super Conducting Laboratory (NSCL), 2016.

[38] B.-M. Sherrill, "Scientific opportunities with the NSCL coupled cyclotron facility," *Progress of Theoretical Physics Supplement*, vol. 146, pp. 60–69, 2002. https://academic.oup.com/ptps/article/doi/10.1143/PTPS.146.60/1864439.

[39] A. W. Chao, K. H. Mess, *et al.*, *Handbook of accelerator physics and engineering*. World scientific, 2013. https://books.google.com/books?hl=en&lr=&id=W4C6CgAAQBAJ&oi=fnd&pg=PR5&dq=Handbook+of+accelerator+physics+and+engineering&ots=696Y_H244C&sig=woigLpWaE_lZKqz35_wyJRnqFRA.

[40] M. Mocko, *Rare isotope production*. PhD thesis, Michigan State University. Department of Physics and Astronomy, 2006. https://groups.nscl.msu.edu/nscl_library/Thesis/Mocko,%20Michal.pdf.

[41] P. van Duppen, "Noyaux exotiques: production propriétés et spécificités," 1997. https://cel.archives-ouvertes.fr/cel-00652717/document.

[42] S. Paschalis, "Studies of exotic nuclei: state-of-the-art experimental tools and techniques," in *Journal of Physics: Conference Series*, vol. 599, p. 012032, IOP Publishing, 2015. https://iopscience.iop.org/article/10.1088/1742-6596/599/1/012032/pdf.

[43] D. J. Morrissey and B. M. Sherrill, "Radioactive nuclear beam facilities based on projectile fragmentation," *Philosophical Transactions of the Royal Society of London. Series A: Mathematical, Physical and Engineering Sciences*, vol. 356, no. 1744, pp. 1985–2006, 1998. https://royalsocietypublishing.org/doi/pdf/10.1098/rsta.1998.0260.

[44] T. Otsuka, "Exotic nuclei and nuclear forces," *Physica Scripta*, vol. 2013, no. T152, p. 014007, 2013. https://iopscience.iop.org/article/10.1088/0031-8949/2013/T152/014007/pdf.

[45] D. . J. Morrissey, B. Sherrill, M. Steiner, A. Stolz, and I. Wiedenhoever, "Commissioning the A1900 projectile fragment separator," *Nuclear Instruments and Methods in Physics Research Section B: Beam Interactions with Materials and Atoms*, vol. 204, pp. 90–96, 2003. https://www.sciencedirect.com/science/article/pii/S0168583X02018955.

[46] K. M. McElroy, "Measurement of fragment transmission in the A1900 fragment separator," https://pdfs.semanticscholar.org/54b9/37247076336583001e296f0e4f56f30bffe7.pdf.

[47] T. Baumann, "Minicourse on experimental techniques at the NSCL fragment separators," 2001. https://people.nscl.msu.edu/ baumann/frs_lecture.pdf.

[48] A. Stolz, T. Baumann, T. Ginter, D. Morrissey, M. Portillo, B. Sherrill, M. Steiner, and J. Stetson, "Production of rare isotope beams with the NSCL fragment separator," *Nuclear Instruments and Methods in Physics Research Section B: Beam Interactions with Materials and Atoms*, vol. 241, no. 1-4, pp. 858–861, 2005. https://www.sciencedirect.com/science/article/pii/S0168583X0501339X.

[49] B. S. Ninel Nica, "Electron capture decay of ^{34}Cl," 2012. https://www.nndc.bnl.gov/nudat2/decaysearchdirect.jsp?nuc=34CL&unc=nds.

[50] N. Nica and B. Singh, "Nuclear data sheets for A= 34," *Nuclear data sheets*, vol. 113, no. 6-7, pp. 1563–1733, 2012. https://www.sciencedirect.com/science/article/pii/S0090375212000488.

[51] K. Heyde and J. L. Wood, "Shape coexistence in atomic nuclei," *Reviews of Modern Physics*, vol. 83, no. 4, p. 1467, 2011. https://link.aps.org/pdf/10.1103/RevModPhys.83.1467.

[52] O. Tarasov and D. Bazin, "LISE++: Exotic beam production with fragment separators and their design," *Nuclear Instruments and Methods in Physics Research Section B: Beam Interactions with Materials and Atoms*, vol. 376, pp. 185–187, 2016. https://www.sciencedirect.com/science/article/pii/S0168583X1600224X?casa_token=G-o0KWEVBJ6UAAAAA:tkupTPZ7L6fwcavNsxiXoDZlCJoaZwx4DEeSAPAfAN3MpG-WO4ja1Vz7hPaYnPaCQ3tVHWeUpqf1T.

[53] C. Meeks and P. Siegel, "Dead time correction via the time series," *American Journal of Physics*, vol. 76, no. 6, pp. 589–590, 2008. https://aapt.scitation.org/doi/pdf/10.1119/1.2870432.

[54] H. J. J. Cleaves, *Branching Ratio*. Springer Berlin Heidelberg, 2011. https://doi.org/10.1007/978-3-642-11274-4_206.